AERODYNAMIC FACILITIES

SECTION 373

Internal Memorandum CP-4

LOAD DISTRIBUTIONS ON THE SURFACE OF PARABOLOIDAL REFLECTOR ANTENNAS

Norman L. Fox

Richard D. Wood

Richard D. Wood, Supervisor
Aerodynamic Testing Group

Robert E. Covey

Robert E. Covey, Chief

Copy No. 117

Jet Propulsion Laboratory
California Institute of Technology
Pasadena, California
July, 1962

CONTENTS

TABLES

FIGURES

FIGURES (Cont'd)

FIGURES (Cont'd)

FIGURES (Cont'd)

ABSTRACT

20616

Pressure distributions over the surfaces of a thin paraboloid of revolution adjacent to a ground plane have been measured. Data are presented for solid, rim-porous, and uniformly porous paraboloidal surfaces at several angular attitudes relative to the ground plane. Integrations of these pressure data over the areas are compared with directly-measured force and moment data. A strong localized edge-loading was found for the solid surface configuration when nearly edge-on to the wind; surface porosity relieved this condition. This material comprises a more detailed presentation of the results from a wind-loads test on paraboloidal reflector antenna models, previously summarized in JPL Internal Memorandum CP-3.

Author

I. INTRODUCTION

One of the design criteria for a paraboloidal reflector directional antenna is reflecting surface position accuracy. This accuracy requirement originates from reflected radio-frequency beam considerations, and is essentially proportional to operating frequencies and independent of reflector diameter. In order to realize the apparent benefits of larger antenna reflector diameters, without imposing restrictive upper frequency limitations, an increasingly careful examination must be made of all the factors affecting this surface position.

One contributing factor to the elastic deflection of the paraboloidal reflecting surface and its supporting structure consists of wind-load distribution over the surface. A portion of the wind tunnel model test to determine wind loads for structural design purposes was, therefore, devoted to measuring pressure distributions over the paraboloidal surface. This paper presents data resulting from the pressure-measurement phase of that test.

Reference 1 summarizes the referenced wind tunnel test performed in the Northrop Subsonic Wind Tunnel in November, 1961. The reader is referred to that Paper for an over-all description of the test equipment, procedures, and nomenclature definitions.

II. TEST DESCRIPTION

Figures 1 and 2 consist of photographs of the pressure-distribution-measurement model. This model consisted of a specially instrumented paraboloidal reflector, otherwise identical to one of the 18-in. -diam models used for

the direct force-moment measurements. It was mounted in the wind tunnel test section in the same position and on the same support strut as the force-moment models. Tests were performed under the same condition, nominally 95-lb/ft^2 dynamic pressure at atmospheric static pressure, yielding a reflector-diameter Reynolds No. 2.7×10^6.

The paraboloidal reflector had a focal-length-to-diameter ratio of 0.330, corresponding to a depth-to-diameter ratio of 0.1894. The thickness of this reflector was 0.007 of the diameter except where the pressure tubes (soldered to the surface) protruded. The basic configuration had a uniform surface porosity of 25% (except for the center 4-in.-diam hub mounting area), consisting of evenly spaced holes with a diameter equal to 0.021 of the reflector diameter. The porosity hole-diameter Reynolds No. was 5.6×10^4. Two other configurations were also tested; one with a solid-surface reflector, and one 25% porous on the outside 1/4 of the radius. These two were simulated by applying pressure-sensitive tape to both sides of the porous surface of the first configuration, and carefully cutting away the tape around the pressure taps. It was inferred from previous portions of the force-moment data, that the surface roughness resulting from this tape would not appreciably effect the resulting data.

Pressures were measured at twenty-two locations on opposite halves of the convex and concave surfaces of the paraboloidal reflector (Fig. 3). This spacing was chosen to roughly represent equal areas per pressure orifice. The inset on Fig. 2 shows the detail of the pressure taps; the metal tubing was soldered to the opposite surface of the reflector. Figure 2 shows the plastic

tubing connected to the metal tubes and leading down through the floor of the wind tunnel test section. Two scanivalves (pneumatic switches), located immediately under the floor, incorporated ±1 psig pressure transducers from which digitized data were automatically recorded. The reference pressures from the tunnel static and total pressure piezometer rings were also connected to these scanivalves and were used in reducing the data to coefficient form. During data reduction, these data were corrected for tunnel static and total pressure calibrations.

III. PRESENTATION OF RESULTS

Data were obtained for model attitudes, with regard to the wind direction, throughout the range of pitch and yaw angles (corresponding to elevation and azimuth angles, respectively). Only the portions of it taken at 0- and 180-deg yaw angles throughout the pitch-angle range are being presented here. The remainder of this data, in rough unchecked form, can be made available on specific request. By means of the side-to-side symmetry, the data is presented exclusively for the 0-deg yaw angle; some of it originated from 180-deg yaw angle and all of it can be interpreted for the latter condition (Fig. 4).

The measured pressures were reduced to the conventional aerodynamic pressure coefficient* form with no tunnel test-section blockage corrections being applied. In all cases these pressures were read two or more nonconsecutive

*Definition of terms used in this report are listed in the Nomenclature.

times. Erroneous values were rejected by cross-plotting and inspection and the remaining values averaged. These remaining values displayed a coefficient scatter bandwidth of as much as 0.05 when the flow was steady. This band increased to as much as 0.21 when the flow (and probably forces) were obviously pulsating or on the edge of a relatively steep gradient.

Tables 1, 2 and 3 present tabulations of the resulting pressure coefficients C_p and the difference of the pressure coefficients ΔC_p for corresponding positions on the concave and convex surfaces of the reflector (from opposite halves by symmetry). The tabulations are arranged by position on the surface, reflector angular attitude, and reflector surface porosity. Figure 3 defines these surface positions, while Fig. 4 defines the model angular attitudes and should further clarify the surface pattern positions at the various model attitudes.

Figures 5 through 21 present in graphical form the pressure-coefficient difference (ΔC_p) across the reflector surface. The abscissas on these plots are the full diametral lines shown in the corresponding colors of Fig. 3, the side-to-side symmetry mentioned above again being applicable.

The integral of the pressure coefficient over any closed surface (with proper regard for vector orientation and moment arm as applicable), represents the major component of the force or moment on that body. Based on a perfect mathematical paraboloid of revolution with zero thickness and no support, these averaged experimental pressure-coefficient differences have been integrated on a digital computer, utilizing mathematical higher-order curve fairing between data points. (Note that these mathematical fairings used for

integrations are not necessarily coincident with the fairings shown on Fig. 5 through 21). The results of these integrations are shown in Fig. 26 through 28. Line fairings of the data from corresponding configurations and model attitudes of the directly-measured force and moment phase of the test are presented in the same colors for compárison.

Throughout this report, experimental results from the pressure data are shown as symbols. Intermediate fairings are judged the best based on comparisons with other types of data from this work and other reports.

IV. DISCUSSION OF RESULTS

Comparison of the results of pressure-data integrations with the directly measured force-mement data is made in Fig. 26 to 28.

Three factors have contributed to the lack of comparisons shown, over and above experimental scatter in both sets of data:

1. Such pressure integrations do not include any contributions from skin friction (i.e., the friction "drag" of the air component blowing locally parallel to the surfaces). In most cases, this contribution is small relative to the pressure-area contribution. Analysis of this contribution is quite difficult for the configurations in question as the flow-field is not well defined. It is significant to note that contributions from skin friction would be affected by surface roughness, and the force-moment phase of the test indicated that surface roughness had little effect on the over-all forces and moments.

2. As noted above, the pressure integrations are based on an ideally shaped surface, and specifically do not include effects of the model reflector thickness, supporting device, center distortion (due to the mounting) and model imperfections.
3. The geometric positions at which pressures were measured may not have yielded continuously adequate definition for such integrations. This is particularly true in the case of localized pressure peaks (Fig. 6) on the edge of the solid surface reflector at approximately 105 deg. The effect is probably greatest for the pitch-moment coefficient comparisons where the moment arm contribution aggrevates edge effects.

The discrepancies itemized above should have little effect on the load distribution curves; as a consequence, the comparisons of Fig. 26, 27, and 28 are considered satisfactory.

In the case of porous surfaces, another factor arises. Around each hole of the porosity, there will be a nonuniform local surface-pressure field, characteristic of flow through the hole. As the inset on Fig. 2 shows, the pressure taps were located midway between porosity holes. The problem then arises of how to perform the pressure-area integration without the details of this local phenomena.

Based on comparisons of the integrated pressure data for axial force, with the corresponding directly-measured axial force, it appears that the best comparisons are obtained by using the remaining solid area; i.e., in the case

of the 25% uniformly porous configuration, 75% of the aperture area. However, in the case of the normal force, the best comparisons are obtained by using the total area and disregarding the porosity. This approach can be somewhat justified by the following viewpoint: for axial force, the vector direction is most nearly perpendicular to the surface, while for normal force, it is most nearly parallel. When the component of interest is almost perpendicular to the surface, the air will "leak" through the holes, causing a load reduction. However, when the component of interest is nearly parallel to the surface, the porosity merely acts as surface roughness. All the comparisons shown for axial force and the axial force component of pitch moment incorporate a 75% factor (one minus the porosity) for porous areas and 100% factor for the solid areas. The 100% factor was used for the normal force and normal force component of pitch moment independent of the porosity. This approach may not be entirely adequate near the border of the porosity in the rim porous configuration, where the plotted pressure coefficient differences suggest the possibility of a discontinuity (Fig. 10 through 14); however, it seems to be the best currently available for estimating local wind-load distributions in this area.

As previously stated, Fig. 6 shows a strong pressure-difference peak near the edge of the solid surface reflector at a 60-deg pitch angle. Inspection of the corresponding pressure coefficients in Table 1 shows that this is the result of a strong negative pressure on the convex (downwind) surface. Comparisons of the pressure-data integrations with the directly-measured force and moment data (Fig. 26 to 28) show somewhat less satisfactory correlation at 60-deg pitch angle than for the other model attitudes. This comparatively poor

correlation is probably related to the localized pressure peak and aggrevated by the large spacing of the pressure orifices.

The presence of this pressure peak and the shape of the force-and-moment curves in this region may be related to a not uncommon aerodynamic phenomena. The parabola, as defined by a focal-length-to-diameter ratio of 0.330, is edge-on to the wind (at infinity) at a pitch angle of 53 deg. The flow-field modification caused by the remainder of the parabola will locally alter this angle by a few degrees. An essentially linear relationship between pitch angle and the forces and moments may be seen in Fig. 26 to 28, particularly for the solid-surface reflector between pitch angles of 55 and 80 deg. In this region, the reflector surface is acting much as a thin-edged circular-arc lifting airfoil; 55 deg corresponding to the positive lift-stall wing condition, and 80 deg to the negative lift-stall wing condition. The force-and-moment peaks observed in the vicinity of 60 deg then must correspond to positive wing stall on a thin leading-edge wing. Initial leading-edge separation, with an attendant localized high negative-pressure peak, is typical in such cases. The air "leaking" through a porous surface has an effect similar to thickening and rounding the sharp leading edge, thus alleviating this leading-edge stall condition.

The above discussion of the wing-leading-edge-stall phenomena has been confirmed by another technique. Figures 22 through 25 present photographs of the model being tested with short tufts of yarn scotch-taped to the reflector surfaces. These tufts respond to the wind adjacent to the surface, and thereby visually indicate the direction of the local air flow. Observe the rows of tufts immediately above and below the reflector mounting hub near the upwind edge of

the reflector. As the antenna was yawed from 55 through 65 deg (by symmetry, equivalent to pitch angles of 55 through 65 deg for which equivalent photographs were not obtained), progressively more of the tufts are blown in a predominantly downstream direction indicating normal attached flow. The tufts near the leading edge (shown blowing upstream) indicate a region of "abnormal" flow that is the separated region of the leading-edge-stall. Several of the tufts right at the leading edge were apparently entangled in the tape and are shown immovable.

The discussion of leading-edge separation applies almost exclusively to the solid-surface reflector. As may be seen by comparing Fig. 6 and 11, the presence of surface porosity on the rim alleviates these pressure peaks. Figures 26 to 28 show a corresponding smoothing and peak reduction of the forces and moments in this region. The air, with a relatively low velocity energy after "leaking" through these porosity holes, provides a smoothing cushion to the flow over the downwind side of the wing or the paraboloidal reflector surface.

No data are available to show the effect of structural members near the convex surface of the reflector on such pressure peaks. Comparisons of force and moment data from this test (not currently published) make it appear that the simulated structure (Fig. 3, Ref. 1) on a solid surface reflector does not alleviate this problem and may aggrevate it.

The results of integrating this pressure-distribution data have been utilized in another way. The faired line data of Fig. 28 shows an appreciable positive pitching moment at 0 deg pitch angle. The pressure distributions of Fig. 5, 10, and 15 show that this pitching moment should be slightly negative, as confirmed by the results of the integrations. If the reflector had been tested

far from any surface, this pitch moment would have been zero due to symmetry. Any pitch moment actually present must, therefore, be due to some combination of ground plane flow restraint and/or boundary layer resulting from the ground plane. With regard to pitching moment, these two effects may have opposite signs, but the ground plane effect probably would dominate.

As mentioned earlier, data are presented in this paper exclusively for 0- and 180-deg yaw angles. Based on comparisons (Fig. 9, Ref. 1), the presence of the ground plane appears to have a moderately small influence. Assuming that this moderate influence may be extended to include pressure distributions, the recorded data of this paper may be applied with like accuracy to any antenna angular attitudes where the spherical sum of the yaw and pitch angles are equal to the pitch angle.

V. SUMMARY

The wind load distribution data presented in this paper are primarily intended for direct use by designers. Analysis of the data points out several interesting features:

1. Wind loads per unit surface area fall off toward the edge of the reflector surface for most reflector angular attitudes. This feature should be beneficial from structural integrity or elastic deformation aspects.
2. Rim porosity of the reflector surface will contribute to decreasing the wind loads at the edge of the surface.

3. Rim porosity of the reflector surface largely eliminates the high pressure peaks occurring at particular model attitudes near the edge of the reflector, which are characteristic of sharp-leading-edge curved aerodynamic surfaces.
4. Comparisons of the directly-measured force-and-moment data with the results of integrating the pressure data over the area lends credence to both sets of data and points out problem areas in the directly-measured pitch-moment data.

NOMENCLATURE

Definition of Pressure Coefficients

1. Conventional aerodynamic pressure coefficients (as used in this paper) in any consistent units are:

$$C_p = \frac{\text{(local surface static pressure) - (ambient static barometric pressure)}}{\text{(wind velocity dynamic pressure)}}$$

2. Pressure coefficient differences then become:

$$\Delta C_p = \frac{\text{(concave surface static pressure) - (convex surface static pressure)}}{\text{(wind velocity dynamic pressure)}}$$

in any consistent units at corresponding positions on the concave and convex sides of the reflector surface. When the C_p is shown as positive, the wind loads are pushing the paraboloidal surface back toward its supporting structure (if present, as in the case of most field installations).

3. Wind velocity dynamic pressure is:

$$\frac{\text{(ambient static air density)} \quad \text{(wind velocity)}^2}{2}$$

A table of the wind velocity dynamic pressure, covering usual wind velocities for a sea-level NACA Standard Day, is presented for convenience:

Wind velocity (mi/hr)	Dynamic pressure (lb/ft^2)
0	0.00
10	0.26
20	1.02
30	2.30
40	4.09
50	6.39
60	9.21
70	12.26
80	16.37
90	20.71
100	25.58
110	30.94
120	36.83

REFERENCES

1. N. L. Fox and B. Dayman, Jr., Preliminary Report on Paraboloidal Reflector Antenna Wind Tunnel Tests, Internal Memorandum CP-3, Jet Propulsion Laboratory, Pasadena, California, February 28, 1962.

Table 1. Pressure coefficients on a thin paraboloidal solid surface

Focal length to diameter ratio, 0.330
solid surface

Diameter Reynolds No., 2.7×10^6
0° yaw (azimuth) angle

R/D*	θ°* deg	0° Pitch angle Concave C_p	0° Pitch angle Convex C_p	0° Pitch angle ΔC_p	60° Pitch angle Concave C_p	60° Pitch angle Convex C_p	60° Pitch angle ΔC_p
0.468	15	+0.78	-0.55	+1.32	+0.29	-0.58	+0.87
	45	+0.78	-0.52	+1.30	+0.34	-0.63	+0.97
	75	+0.79	-0.55	+1.33	+0.38	-2.00	+2.38
	105	+0.81	-0.58	+1.39	+0.58	-3.76	+4.34
	135	+0.84	-0.60	+1.44	+0.73	-1.60	+2.32
	165	+0.90	-0.63	+1.52	+0.66	-1.14	+1.80
0.408	15	+0.94	-0.54	+1.47	+0.55	-0.60	+1.16
	45	+0.94	-0.55	+1.48	+0.59	-0.66	+1.25
	75	+0.95	-0.56	+1.50	+0.63	-1.39	+2.02
	105	+0.95	-0.59	+1.54	+0.69	-1.84	+2.53
	135	+0.97	-0.63	+1.60	+0.73	-0.73	+1.46
	165	+0.99	-0.66	+1.65	+0.69	-0.51	+1.19
0.326	15	+0.98	-0.55	+1.53	+0.69	-0.64	+1.33
	45	+0.99	-0.53	+1.52	+0.71	-0.69	+1.40
	75	+0.98	-0.57	+1.55	+0.73	-0.97	+1.70
	105	+0.99	-0.60	+1.59	+0.78	-0.88	+1.66
	135	+1.01	-0.64	+1.64	+0.76	-0.63	+1.39
	165	+1.01	-0.66	+1.67	+0.74	-0.43	+1.17
0.206	15	+1.00	-0.54	+1.54	+0.79	-0.73	+1.52
	75	+1.01	-0.56	+1.57	+0.79	-0.83	+1.62
	105	+1.01	-0.60	+1.61	+0.79	-0.73	+1.52
	165	+1.02	-0.63	+1.65	+0.81	-0.29	+1.10

*See Fig. 3 for definitions of R/D and θ. Typical for entire table.

Table 1 (Cont'd)

Focal length to diameter ratio, 0.330
solid surface

Diameter Reynolds No., 2.7×10^6
0° yaw (azimuth) angle

R/D	θ° deg	90° Pitch angle Concave C_p	90° Pitch angle Convex C_p	90° Pitch angle ΔC_p	120° Pitch angle Concave C_p	120° Pitch angle Convex C_p	120° Pitch angle ΔC_p
0.468	15	+0.19	-0.36	+0.55	-0.41	-0.43	+0.02
	45	+0.11	-0.14	+0.25	-0.40	-0.42	+0.03
	75	-0.25	-0.27	+0.01	-0.38	-0.37	-0.01
	105	-0.34	-0.20	-0.14	-0.36	-0.10	-0.26
	135	-0.27	+0.29	-0.57	-0.35	+0.46	-0.81
	165	-0.24	+0.75	-0.99	-0.35	+0.93	-1.28
0.408	15	+0.17	-0.36	+0.53	-0.40	-0.49	+0.10
	45	+0.08	-0.22	+0.30	-0.38	-0.54	+0.16
	75	-0.33	-0.36	+0.03	-0.37	-0.44	+0.07
	105	-0.36	-0.28	-0.08	-0.35	-0.05	-0.30
	135	-0.31	+0.15	-0.46	-0.35	+0.54	-0.89
	165	-0.27	+0.50	-0.77	-0.33	+0.93	-1.26
0.326	15	-0.03	-0.34	+0.32	-0.38	-0.53	+0.15
	45	-0.06	-0.30	+0.24	-0.38	-0.61	+0.23
	75	-0.34	-0.40	+0.06	-0.36	-0.48	+0.12
	105	-0.38	-0.31	-0.06	-0.36	-0.07	-0.29
	135	-0.35	-0.01	-0.34	-0.37	+0.44	-0.81
	165	-0.30	+0.60	-0.60	-0.34	+0.80	-1.14
0.206	15	-0.22	-0.34	+0.13	-0.37	-0.61	+0.24
	75	-0.35	-0.42	+0.07	-0.36	-0.48	+0.12
	105	-0.37	-0.34	-0.03	-0.36	-0.18	-0.18
	165	-0.32	+0.00	-0.33	-0.36	+0.59	-0.95

Table 1 (Cont'd)

Focal length to diameter ratio, 0.330
solid surface

Diameter Reynolds No., 2.7×10^6
0° yaw (azimuth) angle

180° Pitch angle

R/D	θ° deg	Concave C_p	Convex C_p	ΔC_p
0.468	15	-0.53	+0.42	-0.95
	45	-0.53	+0.21	-0.75
	75	-0.55	+0.08	-0.62
	105	-0.54	+0.07	-0.61
	135	-0.50	+0.06	-0.56
	165	-0.52	+0.07	-0.59
0.408	15	-0.52	+0.60	-1.12
	45	-0.55	+0.47	-1.02
	75	-0.54	+0.37	-0.91
	105	-0.52	+0.33	-0.85
	135	-0.51	+0.31	-0.82
	165	-0.51	+0.32	-0.83
0.326	15	-0.52	+0.77	-1.29
	45	-0.53	+0.72	-1.24
	75	-0.50	+0.63	-1.13
	105	-0.52	+0.58	-1.10
	135	-0.52	+0.58	-1.10
	165	-0.51	+0.56	-1.07
0.206	15	-0.51	+0.84	-1.35
	75	-0.53	+0.82	-1.35
	105	-0.52	+0.79	-1.30
	165	-0.51	+0.82	-1.32

Table 2. Pressure coefficients on a thin paraboloidal porous rim surface

Focal length to diameter ratio, 0.330
Porous rim surface

Diameter Reynolds No., 2.7×10^6
0° yaw (azimuth) angle

R/D*	θ° * deg	0° Pitch angle Concave C_p	0° Pitch angle Convex C_p	0° Pitch angle ΔC_p	60° Pitch angle Concave C_p	60° Pitch angle Convex C_p	60° Pitch angle ΔC_p
0.468	15	+0.81	-0.73	+1.54	+0.25	-0.71	+0.96
	45	+0.83	-0.71	+1.53	+0.29	-0.81	+1.10
	75	+0.84	-0.73	+1.57	+0.45	-0.87	+1.32
	105	+0.87	-0.74	+1.61	+0.60	-1.05	+1.66
	135	+0.90	-0.67	+1.58	+0.58	-1.00	+1.58
	165	+0.94	-0.68	+1.62	+0.42	-0.69	+1.11
0.408	15	+0.88	-0.74	+1.61	+0.42	-0.72	+1.15
	45	+0.91	-0.73	+1.64	+0.49	-0.86	+1.35
	75	+0.92	-0.79	+1.71	+0.58	-0.92	+1.50
	105	+0.92	-0.76	+1.68	+0.68	-1.09	+1.77
	135	+0.95	-0.79	+1.74	+0.68	-1.01	+1.69
	165	+0.97	-0.70	+1.68	+0.63	-0.86	+1.49
0.326	15	+0.94	-0.52	+1.46	+0.60	-0.59	+1.19
	45	+0.97	-0.50	+1.47	+0.64	-0.62	+1.26
	75	+0.96	-0.54	+1.50	+0.69	-0.70	+1.38
	105	+0.96	-0.56	+1.51	+0.73	-0.82	+1.55
	135	+0.99	-0.57	+1.57	+0.76	-0.66	+1.42
	165	+1.00	-0.57	+1.57	+0.75	-0.61	+1.36
0.206	15	+0.99	-0.50	+1.49	+0.75	-0.69	+1.44
	75	+1.01	-0.52	+1.53	+0.77	-0.82	+1.58
	105	+1.01	-0.54	+1.55	+0.77	-0.74	+1.51
	165	+1.02	-0.54	+1.56	+0.80	-0.36	+1.16

*See Fig. 3 for definitions of R/D and θ. Typical for entire table.

Table 2 (Cont'd)

Focal length to diameter ratio, 0.330
Porous rim surface

Diameter Reynolds No., 2.7×10^6
0° yaw (azimuth) angle

R/D	θ° deg	90° Pitch angle Concave C_p	90° Pitch angle Convex C_p	90° Pitch angle ΔC_p	120° Pitch angle Concave C_p	120° Pitch angle Convex C_p	120° Pitch angle ΔC_p
0.468	15	+0.20	-0.35	+0.55	-0.39	-0.42	+0.03
	45	-0.05	-0.18	+0.12	-0.37	-0.43	+0.06
	75	-0.28	-0.35	+0.07	-0.36	-0.39	+0.03
	105	-0.29	-0.21	-0.08	-0.40	-0.11	-0.30
	135	-0.38	+0.28	-0.66	-0.50	+0.48	-0.98
	165	-0.50	+0.74	-1.24	-0.54	+0.94	-1.47
0.408	15	+0.06	-0.35	+0.42	-0.37	-0.41	+0.04
	45	-0.16	-0.17	+0.02	-0.36	-0.42	+0.06
	75	-0.32	-0.40	+0.08	-0.36	-0.42	+0.06
	105	-0.29	-0.28	-0.01	-0.44	-0.07	-0.37
	135	-0.31	+0.08	-0.40	-0.51	+0.52	-1.03
	165	-0.42	+0.55	-0.97	-0.57	+0.95	-1.52
0.326	15	-0.05	-0.31	+0.26	-0.36	-0.44	+0.08
	45	-0.20	-0.25	+0.05	-0.35	-0.48	+0.13
	75	-0.29	-0.36	+0.07	-0.35	-0.36	+0.01
	105	-0.29	-0.27	-0.02	-0.35	-0.01	-0.36
	135	-0.29	+0.06	-0.35	-0.35	+0.51	-0.85
	165	-0.32	+0.38	-0.70	-0.34	+0.84	-1.19
0.206	15	-0.18	-0.33	+0.15	-0.35	-0.52	+0.17
	75	-0.29	-0.40	+0.11	-0.35	-0.44	+0.10
	105	-0.29	-0.32	+0.02	-0.34	-0.11	-0.23
	165	-0.31	+0.21	-0.52	-0.34	+0.63	-0.97

Table 2 (Cont'd)

Focal length to diameter ratio, 0.330
Porous rim surface

Diameter Reynolds No., 2.7×10^6
0° yaw (azimuth) angle

180° Pitch angle

R/D	θ° deg	Concave C_p	Convex C_p	ΔC_p
0.468	15	-0.74	+0.31	-1.06
	45	-0.74	+0.06	-0.80
	75	-0.75	+0.04	-0.80
	105	-0.70	+0.03	-0.73
	135	-0.65	+0.06	-0.71
	165	-0.60	+0.05	-0.65
0.408	15	-0.64	+0.49	-1.13
	45	-0.65	+0.37	-1.03
	75	-0.71	+0.28	-0.99
	105	-0.72	+0.24	-0.95
	135	-0.67	+0.24	-0.91
	165	-0.66	+0.23	-0.89
0.326	15	-0.50	+0.64	-1.14
	45	-0.50	+0.69	-1.19
	75	-0.53	+0.57	-1.09
	105	-0.53	+0.53	-1.06
	135	-0.59	+0.53	-1.12
	165	-0.61	+0.51	-1.12
0.206	15	-0.48	+0.82	-1.31
	75	-0.50	+0.81	-1.31
	105	-0.50	+0.74	-1.24
	165	-0.51	+0.81	-1.32

Table 3. Pressure coefficients on a thin paraboloidal porous surface

Focal length to diameter ratio, 0.330
Porous surface

Diameter Reynolds No., 2.7×10^6
0° yaw (azimuth) angle

R/D*	θ°* deg	0° Pitch angle Concave C_p	0° Pitch angle Convex C_p	0° Pitch angle ΔC_p	30° Pitch angle Concave C_p	30° Pitch angle Convex C_p	30° Pitch angle ΔC_p
0.468	15	+0.93	-0.70	+1.63	+0.66	-0.67	+1.33
	45	+0.93	-0.69	+1.61	+0.70	-0.65	+1.34
	75	+0.95	-0.70	+1.64	+0.78	-0.71	+1.49
	105	+0.95	-0.71	+1.66	+0.87	-0.76	+1.63
	135	+0.97	-0.72	+1.69	+0.94	-0.83	+1.76
	165	+0.99	-0.76	+1.75	+0.95	-1.01	+1.95
0.408	15	+0.99	-0.69	+1.68	+0.84	-0.69	+1.53
	45	+1.00	-0.74	+1.74	+0.87	-0.72	+1.59
	75	+1.00	-0.77	+1.77	+0.89	-0.71	+1.59
	105	+1.01	-0.71	+1.72	+0.92	-0.72	+1.64
	135	+1.01	-0.72	+1.73	+0.91	-0.77	+1.67
	165	+1.02	-0.68	+1.70	+0.90	-0.78	+1.68
0.326	15	+1.00	-0.72	+1.72	+0.90	-0.69	+1.59
	45	+1.01	-0.74	+1.74	+0.92	-0.71	+1.63
	75	+1.01	-0.74	+1.75	+0.91	-0.71	+1.62
	105	+1.01	-0.74	+1.74	+0.91	-0.72	+1.63
	135	+1.02	-0.72	+1.74	+0.91	-0.70	+1.61
	165	+1.02	-0.71	+1.73	+0.91	-0.67	+1.57
0.206	15	+1.01	-0.83	+1.84	+0.93	-0.80	+1.73
	75	+1.00	-0.81	+1.81	+0.93	-0.77	+1.70
	105	+1.02	-0.83	+1.84	+0.94	-0.76	+1.70
	165	+1.02	-0.78	+1.79	+0.94	-0.57	+1.51

*See Fig. 3 for definitions of R/D and θ. Typical for entire table.

Table 3 (Cont'd)

Focal length to diameter ratio, 0.330
Porous surface

Diameter Reynolds No., 2.7×10^6
0° yaw (azimuth) angle

R/D	θ° deg	60° Pitch angle Concave C_p	60° Pitch angle Convex C_p	60° Pitch angle ΔC_p	90° Pitch angle Concave C_p	90° Pitch angle Convex C_p	90° Pitch angle ΔC_p
0.468	15	+0.42	-0.53	+0.94	+0.12	-0.27	+0.40
	45	+0.45	-0.60	+1.05	-0.03	-0.29	+0.26
	75	+0.49	-0.90	+1.39	-0.17	-0.25	+0.07
	105	+0.54	-0.80	+1.35	-0.33	-0.19	-0.15
	135	+0.43	-0.48	+0.91	-0.48	+0.29	-0.77
	165	+0.28	-0.06	+0.34	-0.61	+0.73	-1.33
0.408	15	+0.63	-0.61	+1.24	+0.02	-0.27	+0.29
	45	+0.66	-0.69	+1.35	-0.07	-0.27	+0.20
	75	+0.65	-0.83	+1.48	-0.18	-0.28	+0.09
	105	+0.60	-0.64	+1.24	-0.33	-0.24	-0.09
	135	+0.50	-0.42	+0.91	-0.41	+0.10	-0.51
	165	+0.39	-0.20	+0.59	-0.52	+0.49	-1.01
0.326	15	+0.72	-0.64	+1.35	-0.13	-0.30	+0.17
	45	+0.74	-0.71	+1.45	-0.12	-0.26	+0.14
	75	+0.71	-0.77	+1.48	-0.19	-0.28	+0.09
	105	+0.63	-0.70	+1.33	-0.31	-0.26	-0.05
	135	+0.56	-0.55	+1.11	-0.34	+0.03	-0.37
	165	+0.52	-0.28	+0.80	-0.41	+0.30	-0.71
0.206	15	+0.78	-0.74	+1.52	-0.20	-0.28	+0.08
	75	+0.74	-0.76	+1.50	-0.26	-0.33	+0.06
	105	+0.71	-0.74	+1.45	-0.29	-0.26	-0.03
	165	+0.69	-0.38	+1.07	-0.34	+0.16	-0.50

Table 3 (Cont'd)

Focal length to diameter ratio, 0.330
Porous surface

Diameter Reynolds No., 2.7×10^6
0° yaw (azimuth) angle

R/D	θ° deg	120° Pitch angle Concave C_p	Convex C_p	ΔC_p	150° Pitch angle Concave C_p	Convex C_p	ΔC_p
0.468	15	-0.37	-0.38	+0.01	-0.44	-0.18	-0.26
	45	-0.36	-0.40	+0.04	-0.49	-0.15	-0.34
	75	-0.34	-0.36	+0.02	-0.55	-0.07	-0.48
	105	-0.38	-0.06	-0.32	-0.62	+0.15	-0.77
	135	-0.62	+0.49	-1.11	-0.70	+0.42	-1.12
	165	-0.74	+0.95	-1.69	-0.76	+0.62	-1.38
0.408	15	-0.37	-0.39	+0.02	-0.51	-0.07	-0.44
	45	-0.36	-0.40	+0.05	-0.53	-0.01	-0.52
	75	-0.35	-0.36	+0.00	-0.57	+0.10	-0.67
	105	-0.40	-0.01	-0.39	-0.65	+0.39	-1.03
	135	-0.61	+0.55	-1.17	-0.75	+0.67	-1.42
	165	-0.76	+0.92	-1.68	-0.80	+0.87	-1.67
0.326	15	-0.37	-0.41	+0.04	-0.56	+0.02	-0.58
	45	-0.35	-0.41	+0.06	-0.59	+0.15	-0.74
	75	-0.34	-0.34	-0.01	-0.64	+0.30	-0.94
	105	-0.40	+0.03	-0.43	-0.73	+0.54	-1.27
	135	-0.63	+0.50	-1.13	-0.80	+0.80	-1.60
	165	-0.73	+0.82	-1.55	-0.81	+0.97	-1.78
0.206	15	-0.34	-0.37	+0.03	-0.69	+0.10	-0.79
	75	-0.33	-0.36	+0.03	-0.75	+0.43	-1.18
	105	-0.40	-0.02	-0.38	-0.82	+0.63	-1.45
	165	-0.65	+0.63	-1.27	-0.86	+0.99	-1.85

Table 3 (Cont'd)

Focal length to diameter ratio, 0.330
Porous surface

Diameter Reynolds No., 2.7×10^6
0° yaw (azimuth) angle

180° Pitch angle

R/D	θ° deg	Concave C_p	Convex C_p	ΔC_p
0.468	15	-0.69	+0.37	-1.06
	45	-0.71	+0.24	-0.95
	75	-0.68	+0.16	-0.84
	105	-0.67	+0.14	-0.80
	135	-0.69	+0.13	-0.81
	165	-0.69	+0.13	-0.81
0.408	15	-0.72	+0.62	-1.34
	45	-0.75	+0.51	-1.26
	75	-0.74	+0.44	-1.18
	105	-0.73	+0.40	-1.13
	135	-0.71	+0.38	-1.10
	165	-0.74	+0.38	-1.12
0.326	15	-0.76	+0.71	-1.47
	45	-0.73	+0.74	-1.47
	75	-0.73	+0.65	-1.38
	105	-0.74	+0.64	-1.39
	135	-0.73	+0.60	-1.33
	165	-0.75	+0.59	-1.33
0.206	15	-0.83	+0.79	-1.62
	75	-0.82	+0.79	-1.62
	105	-0.76	+0.79	-1.55
	165	-0.78	+0.83	-1.61

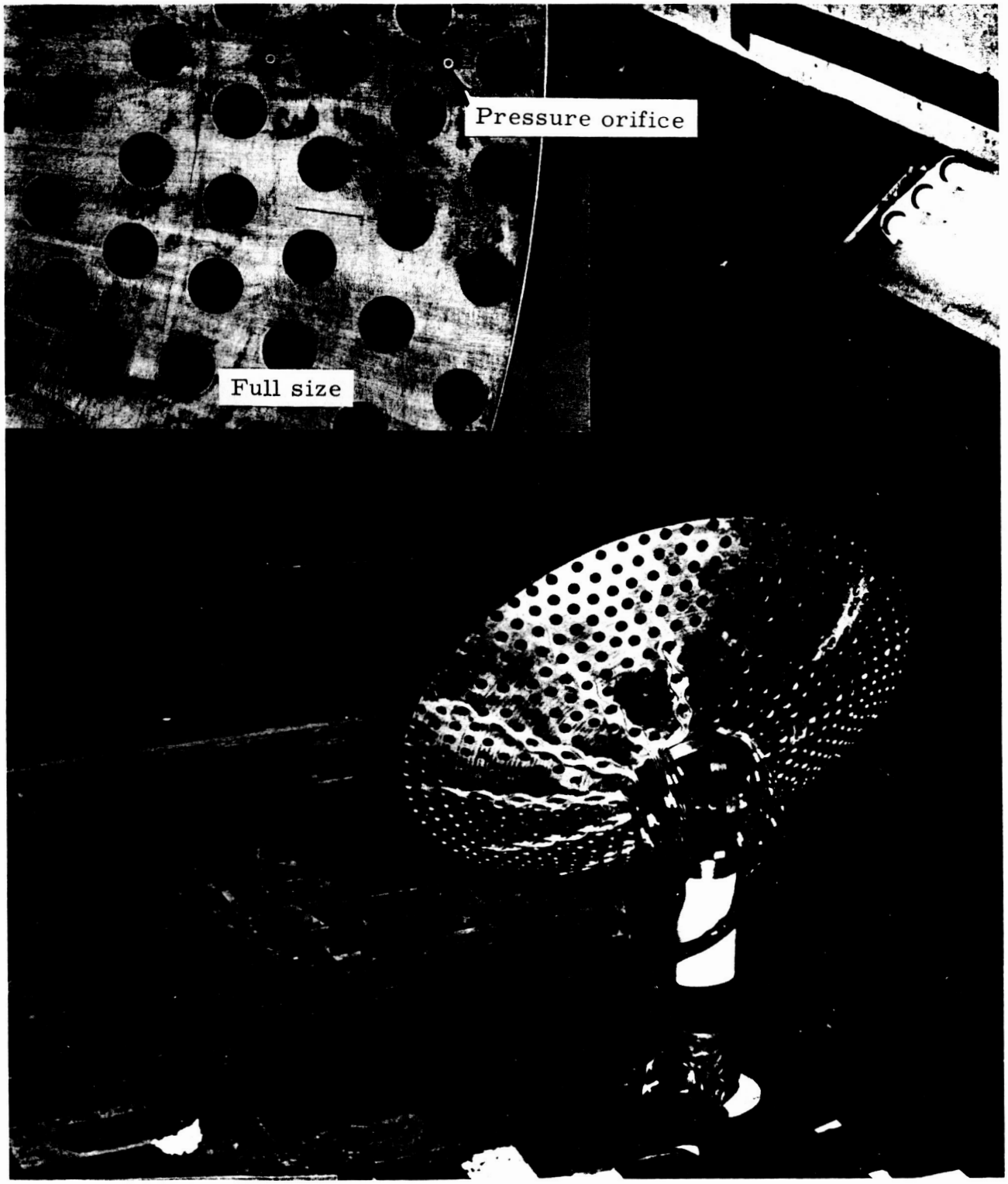

$\frac{\text{Focal length}}{\text{Diameter}} = 0.330$ 25% uniform surface porosity

Fig. 1. Pressure Distribution Measurement Model in Wind Tunnel Test Section.

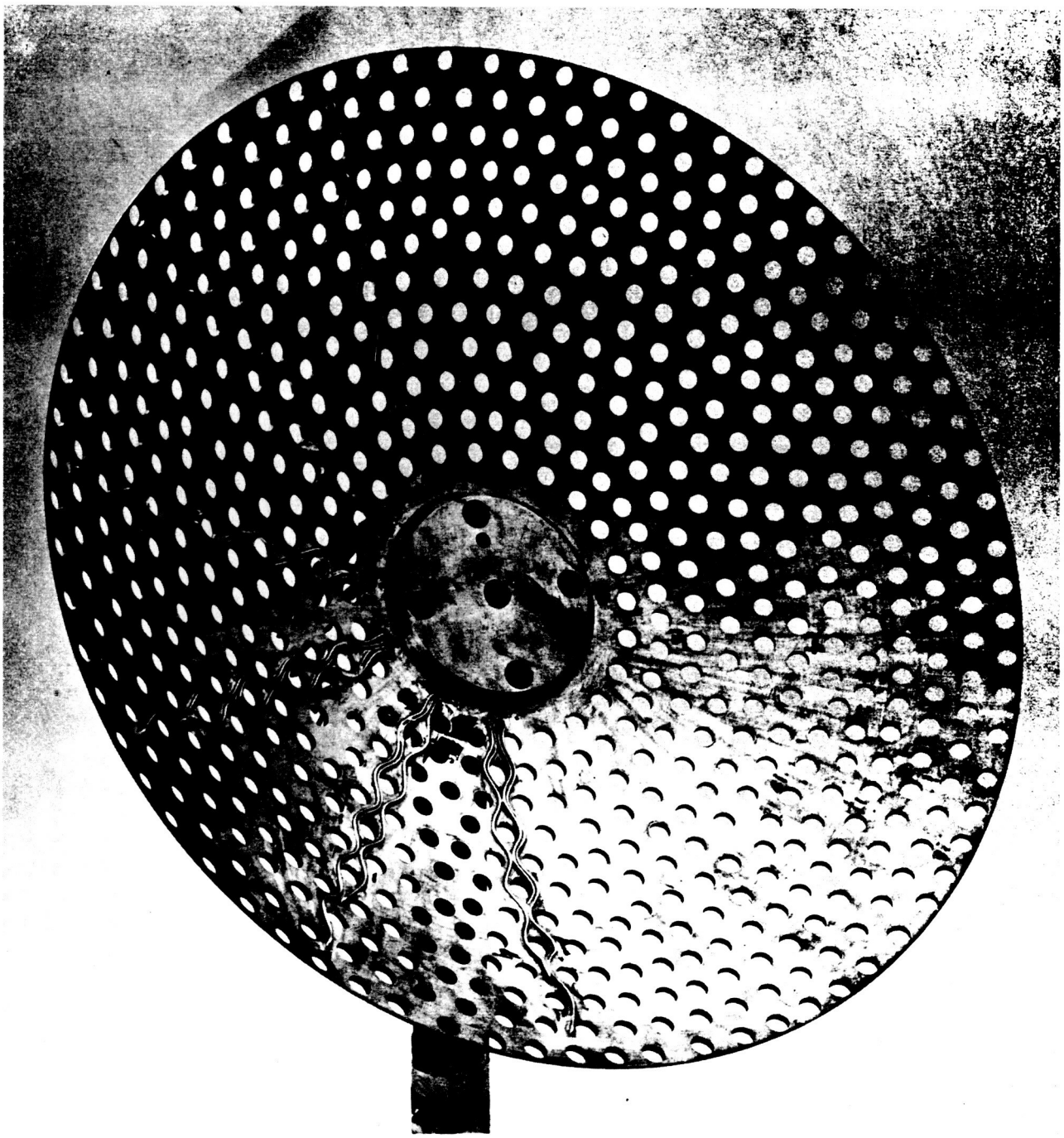

Fig. 2. Pressure Distribution Measurement Model Showing Pressure Taps and Tubing.

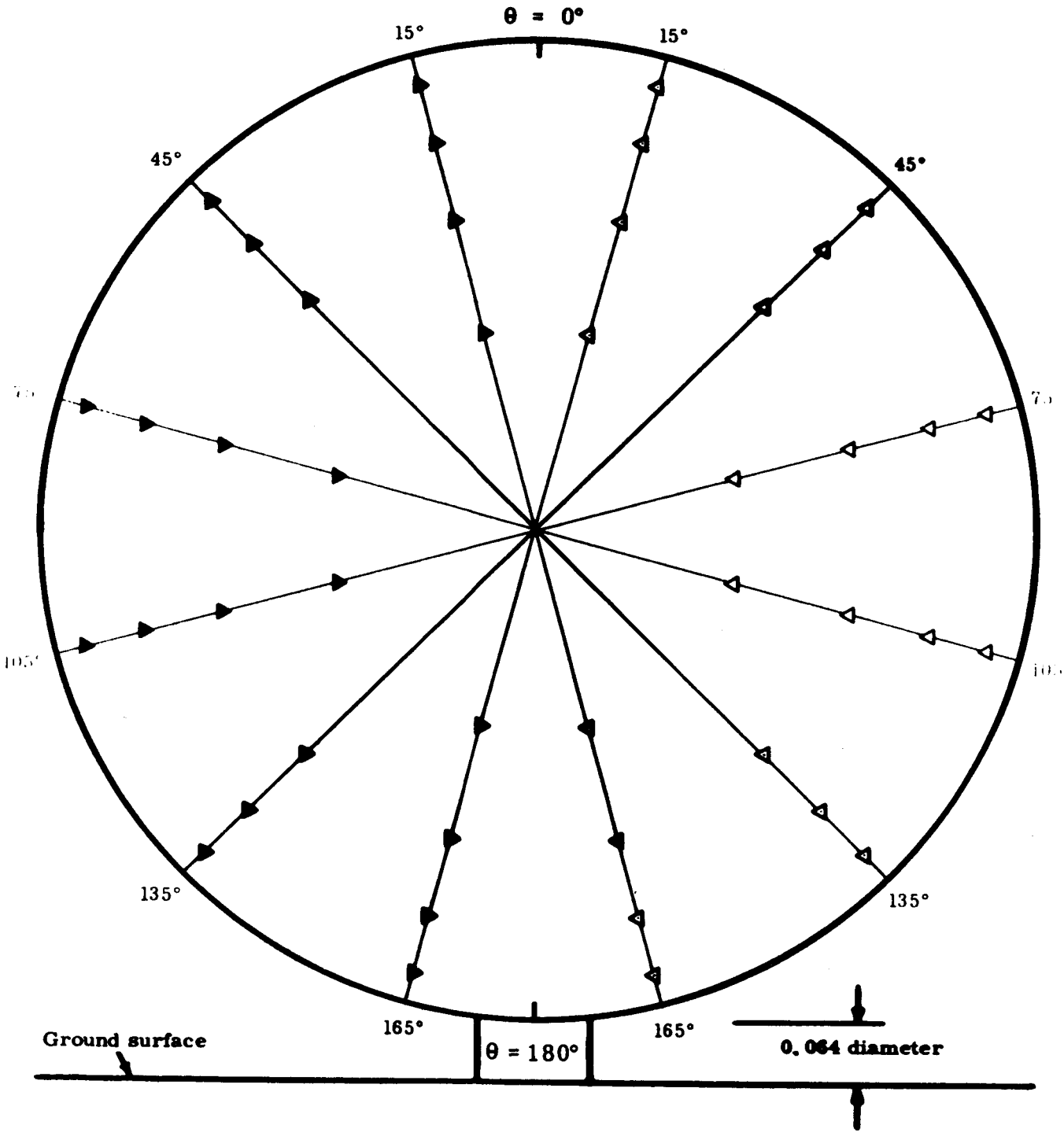

Looking into concave face at zero pitch and yaw angles

◁ **pressure tap on concave surface**
▶ **pressure tap on convex surface**

θ signifies angular position of pressure taps
R/D signifies radial position of pressure taps

Fig. 3. Pressure tap locations on model

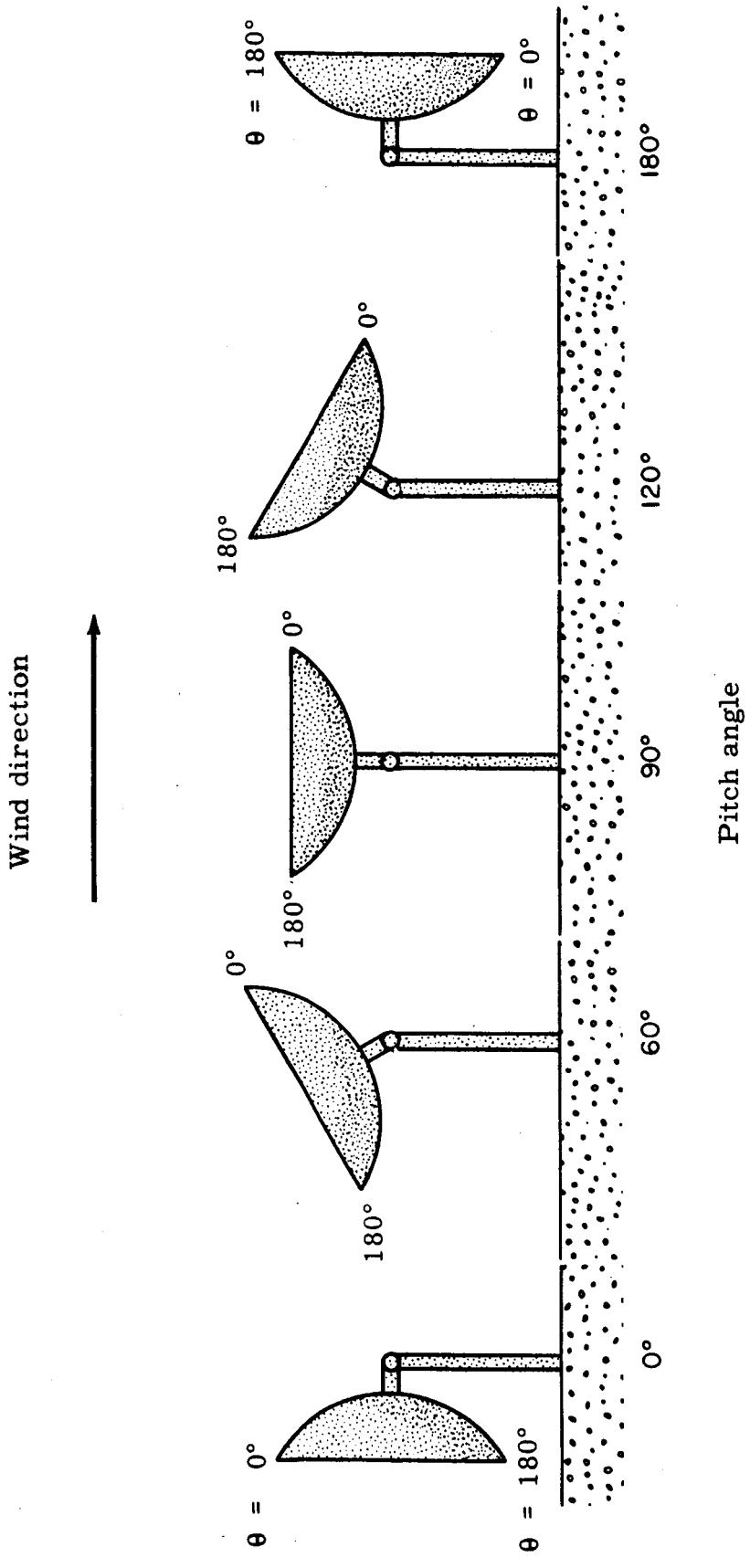

Fig. 4. Paraboloidal reflector antenna model attitudes

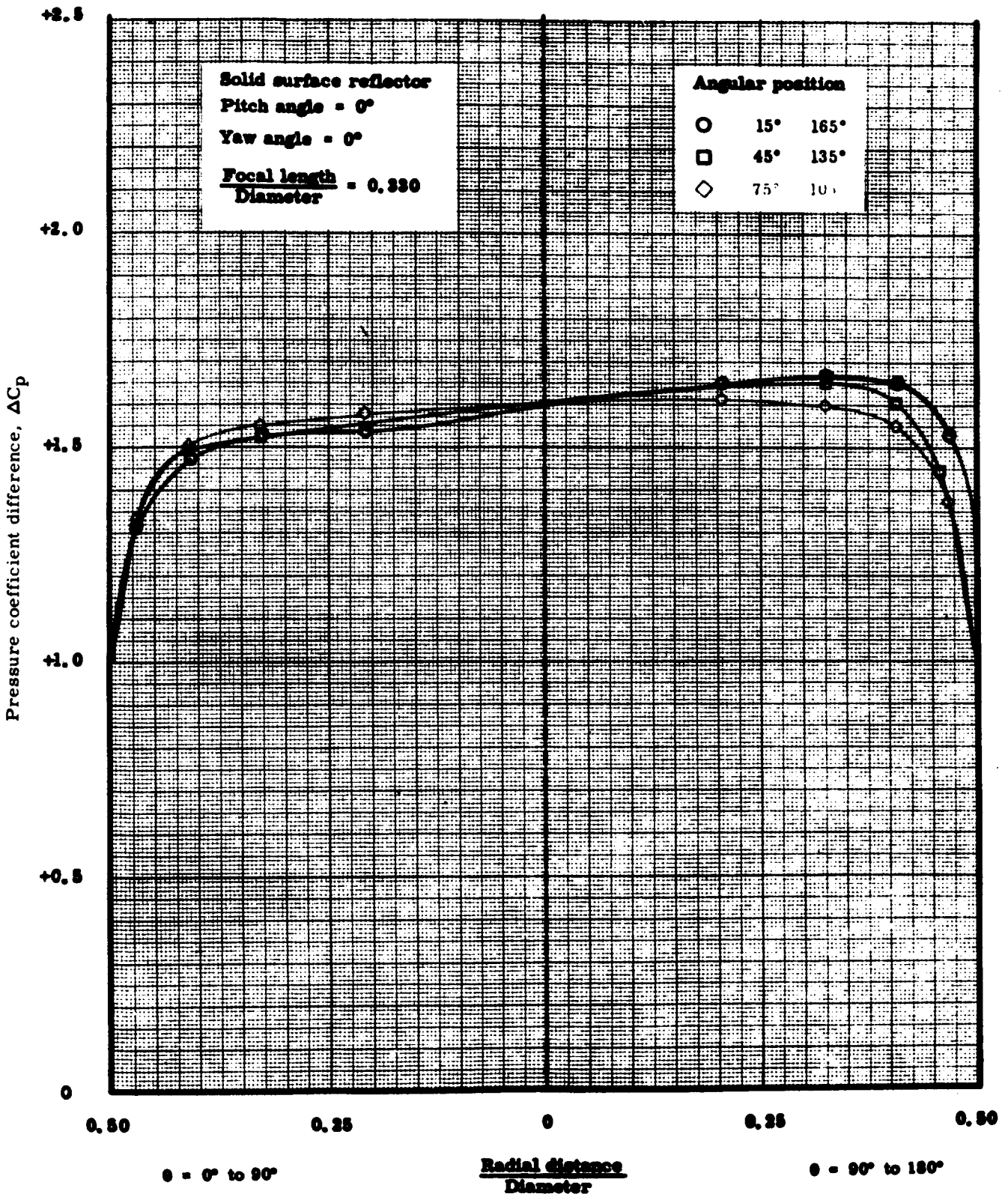

Fig. 5. Pressure coefficient difference across a thin parabolodial surface

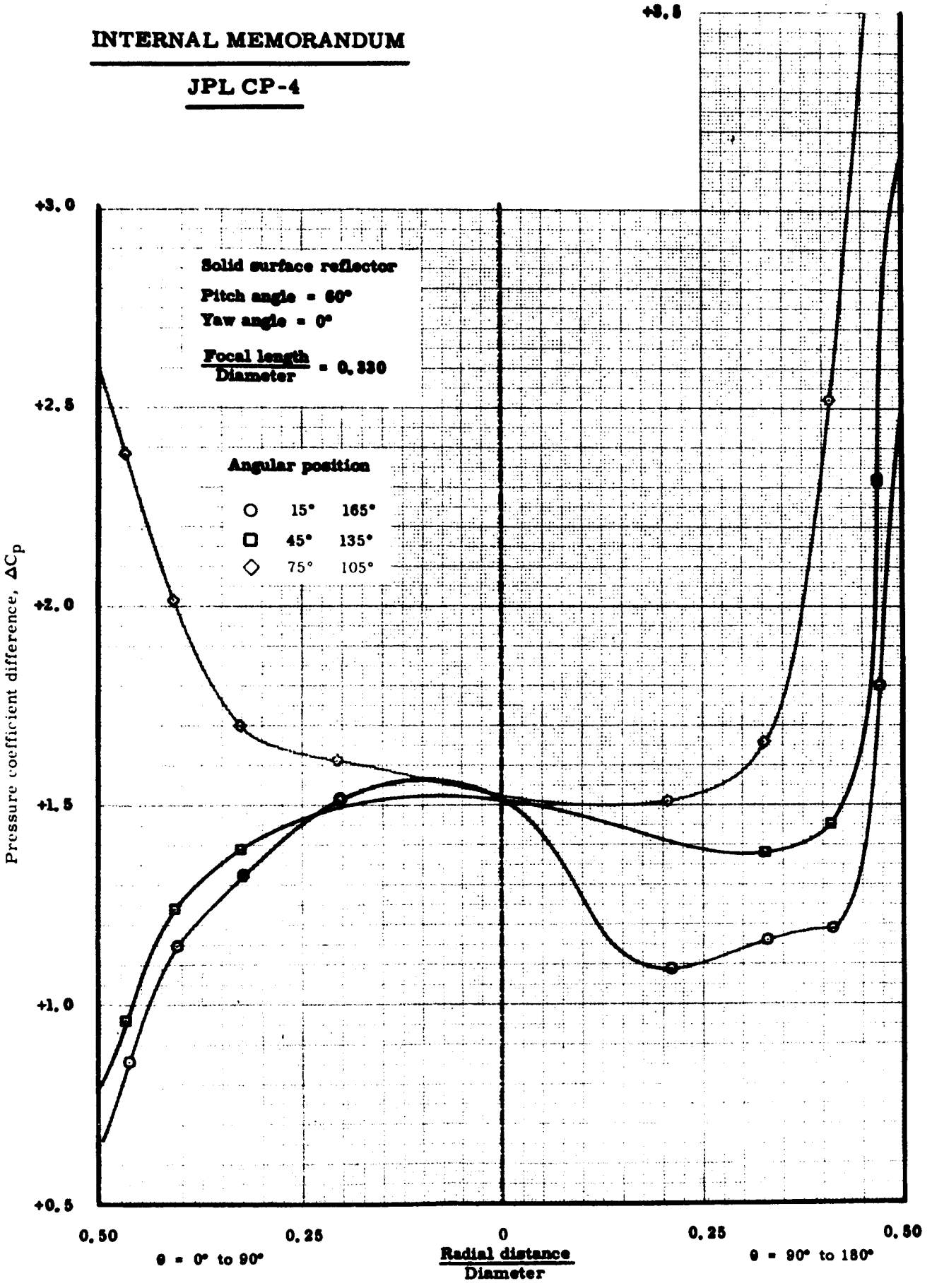

Fig. 6. Pressure coefficient difference across a thin parabolodial surface

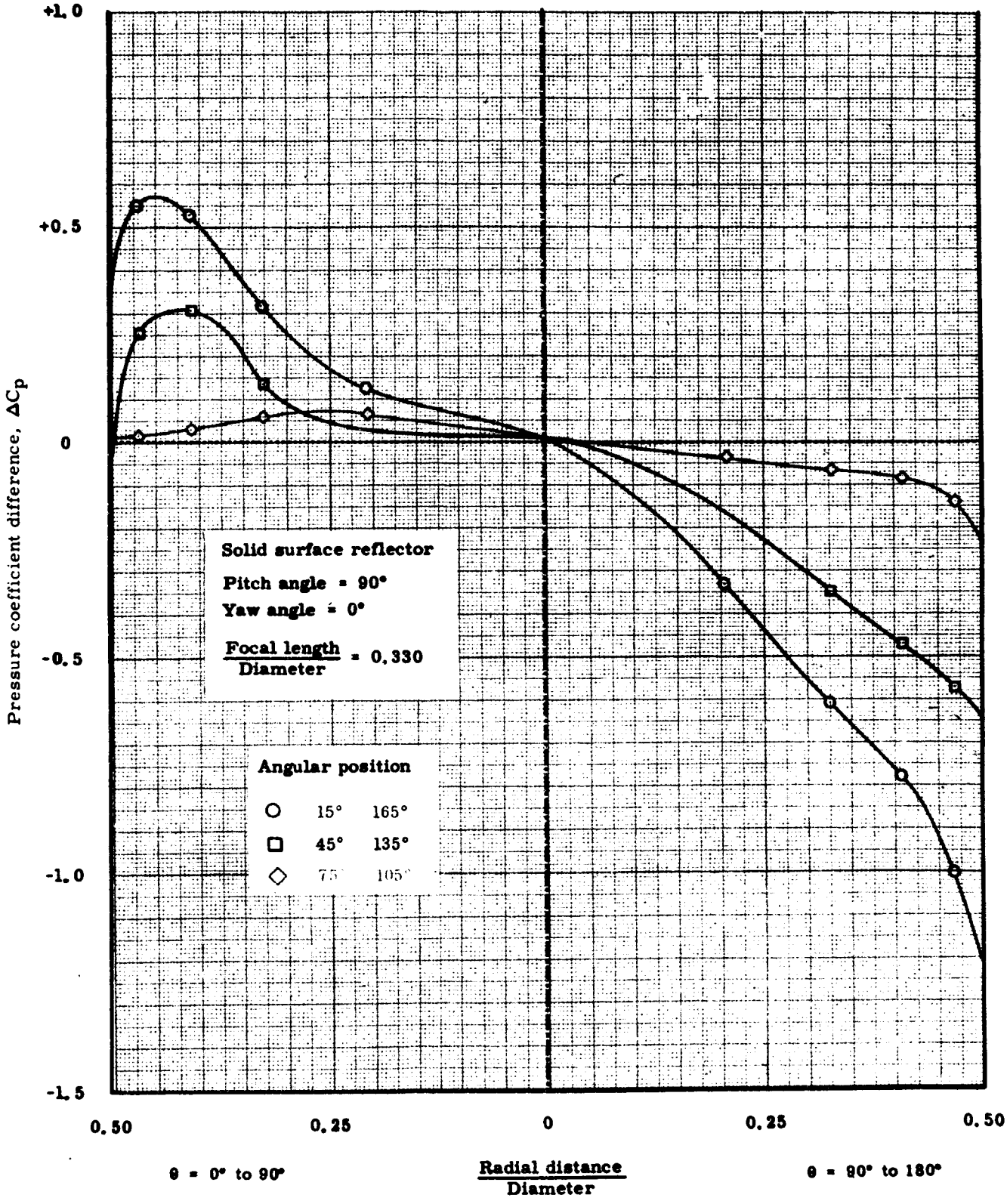

Fig. 7. Pressure Coefficient Difference Across a Thin Paraboloidal Solid Surface, Pitch Angle 90°.

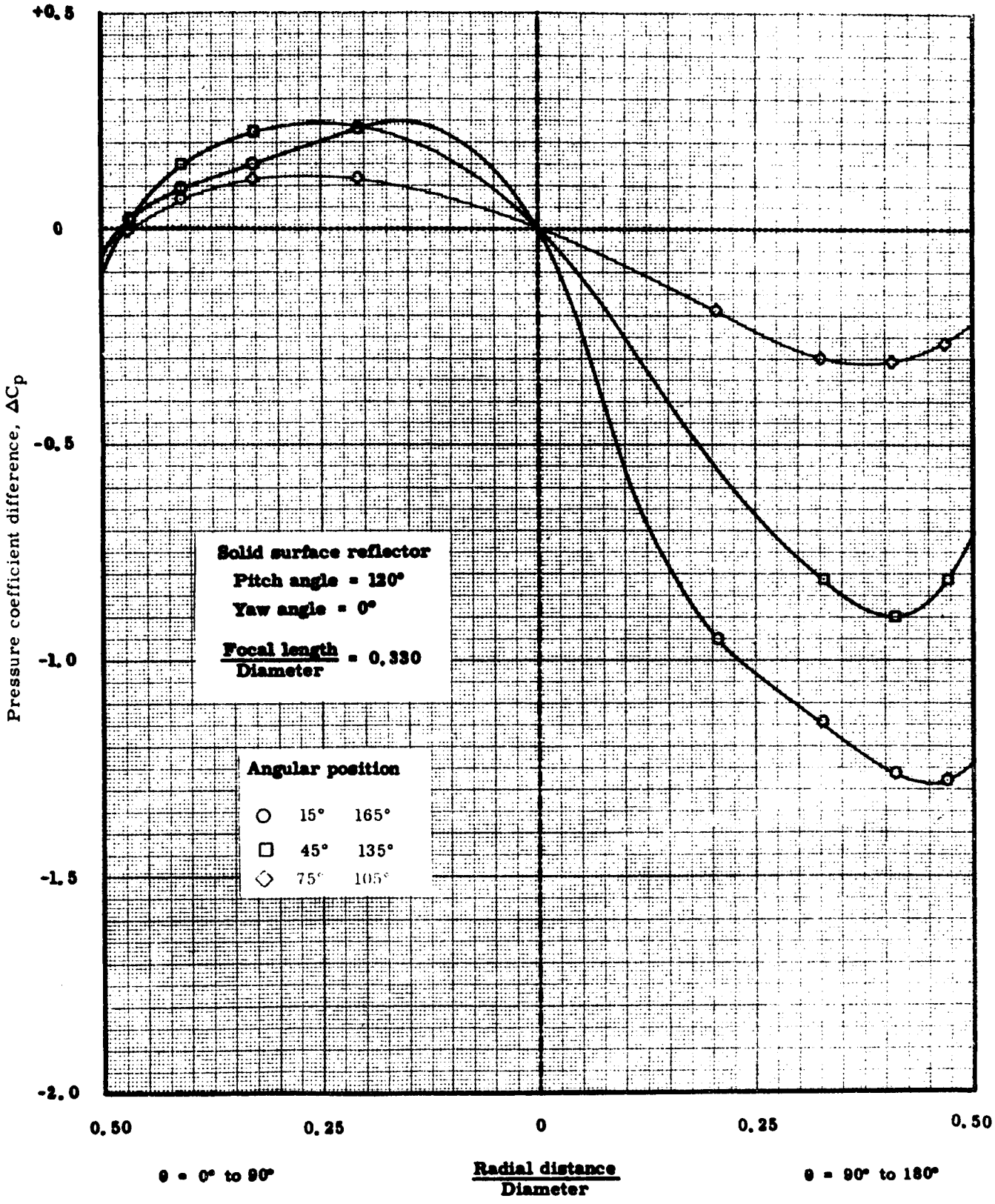

Fig. 8. Pressure Coefficient Difference Across a Thin Paraboloidal Solid Surface, Pitch Angle 120°.

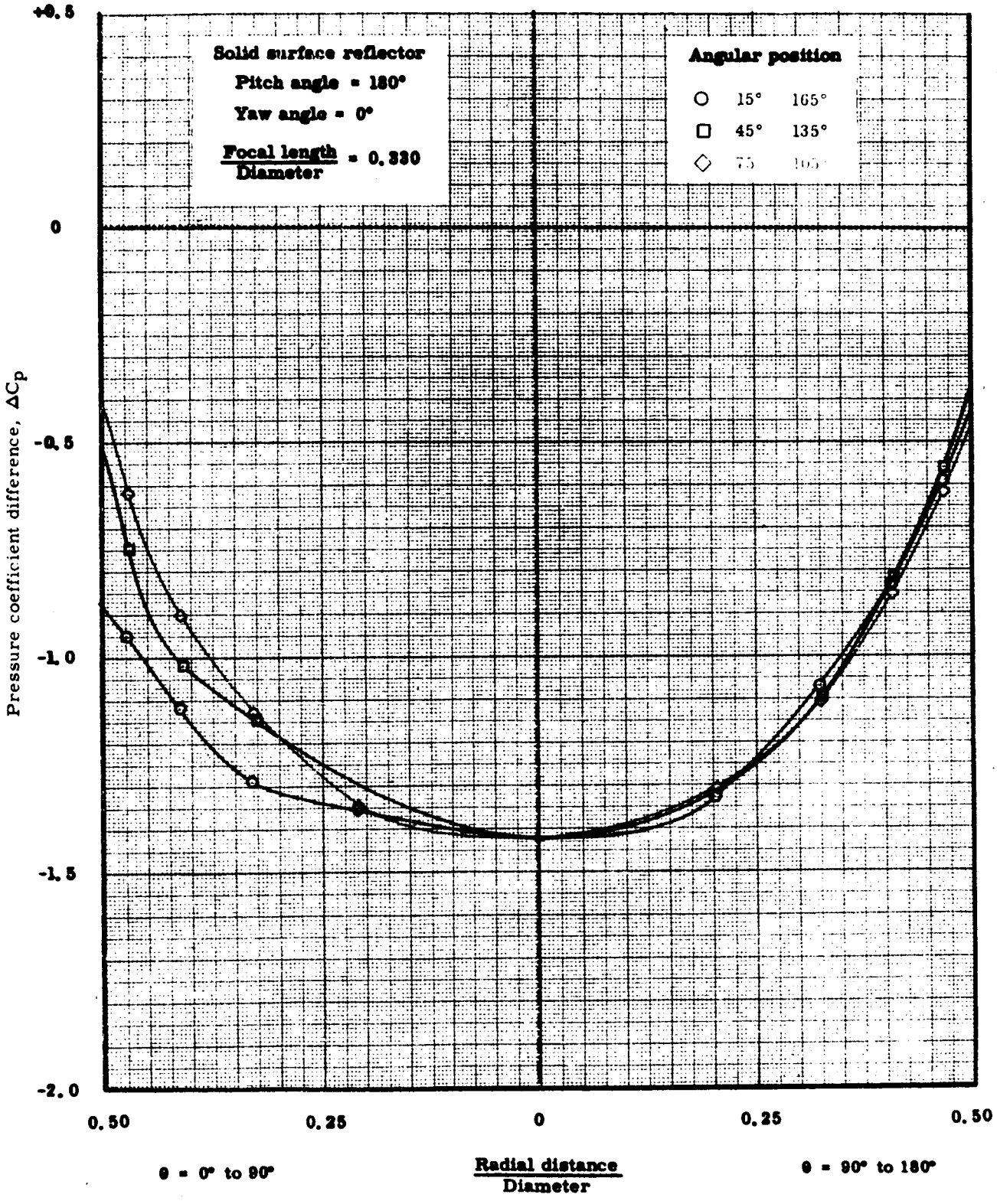

Fig. 9. Pressure Coefficient Difference Across a Thin Paraboloidal Solid Surface, Pitch Angle 180°.

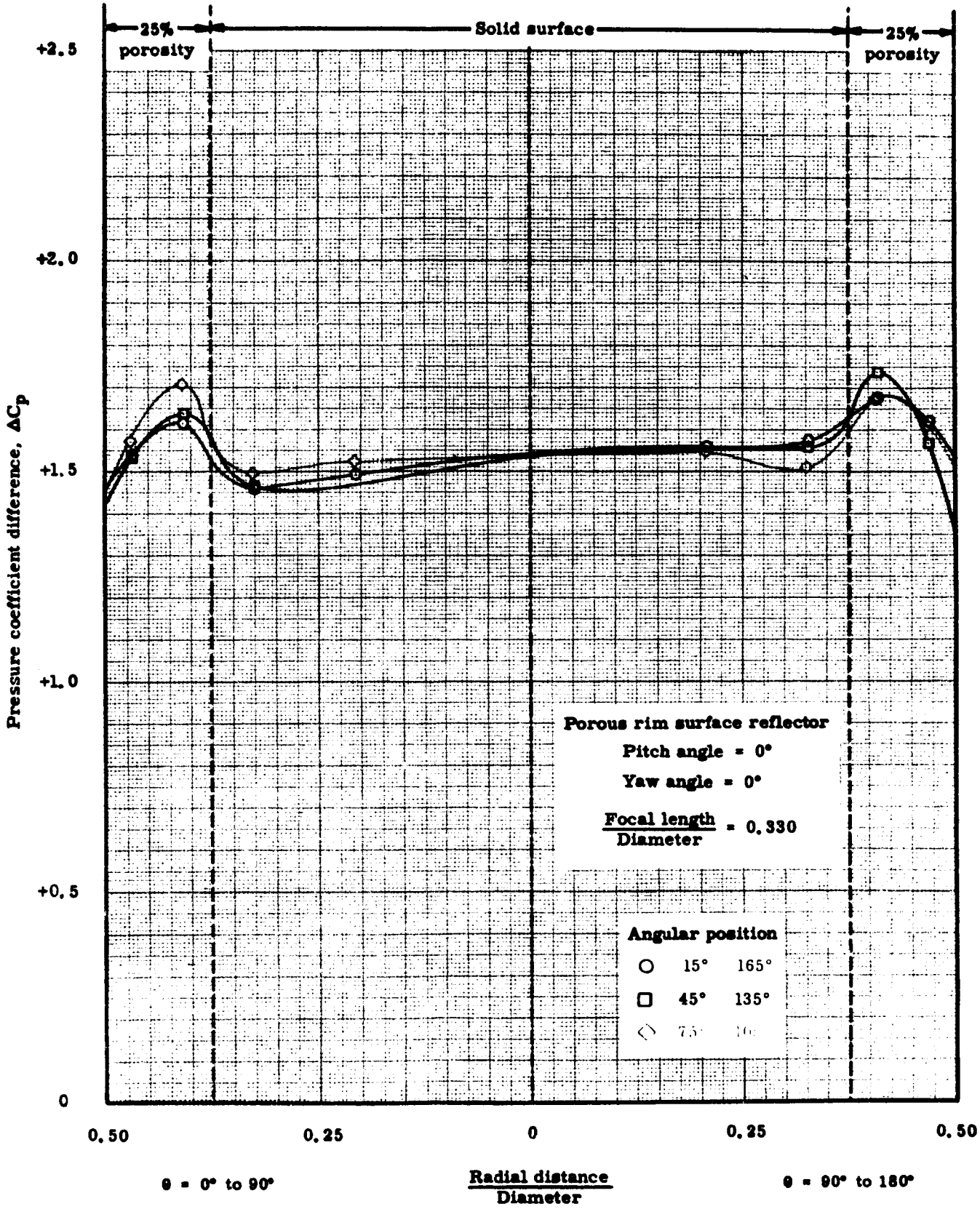

Fig. 10. Pressure Coefficient Difference Across a Thin Paraboloidal Porous Rim Surface, Pitch Angle 0°.

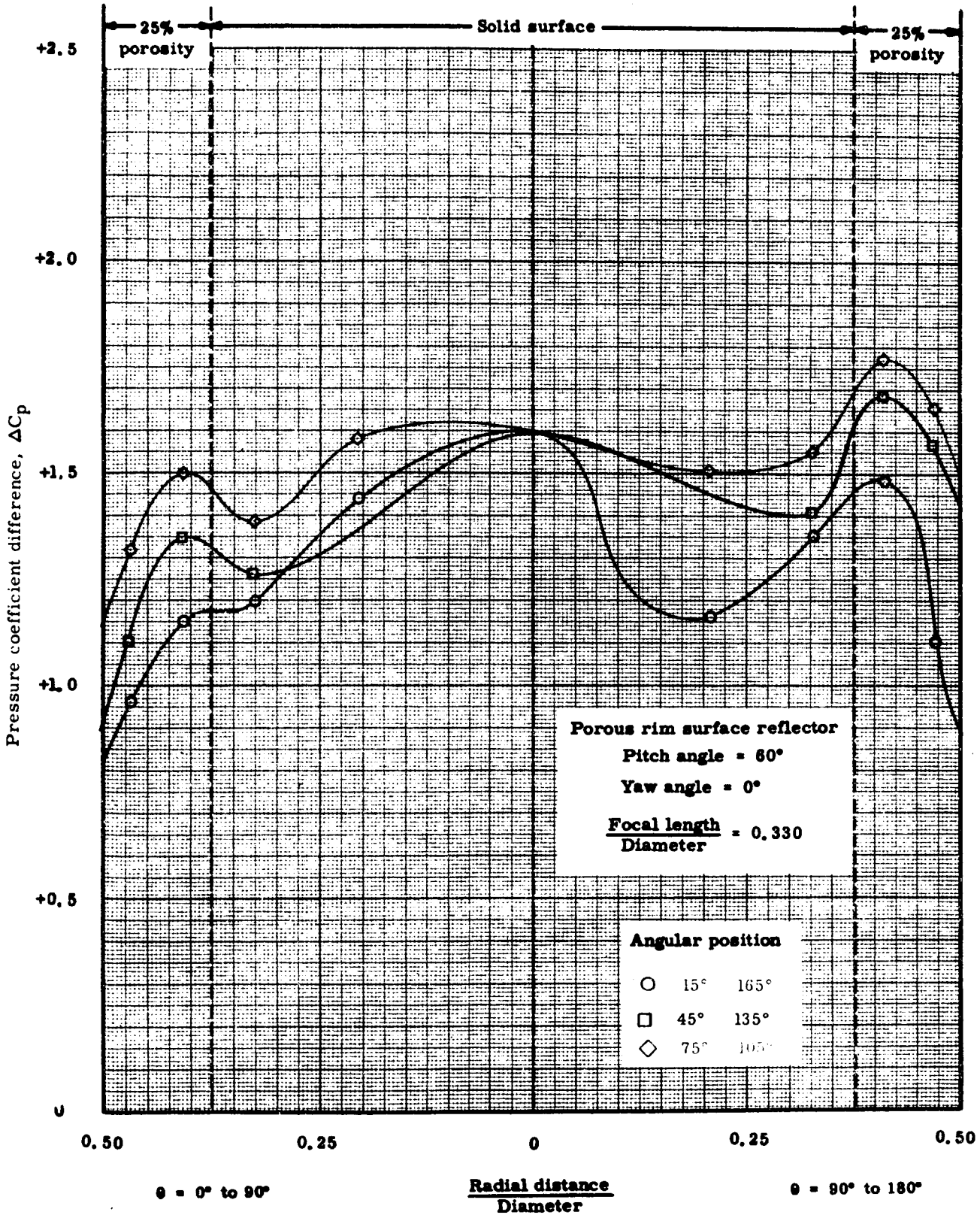

Fig. 11. Pressure Coefficient Difference Across a Thin Paraboloidal Porous Rim Surface, Pitch Angle 60°.

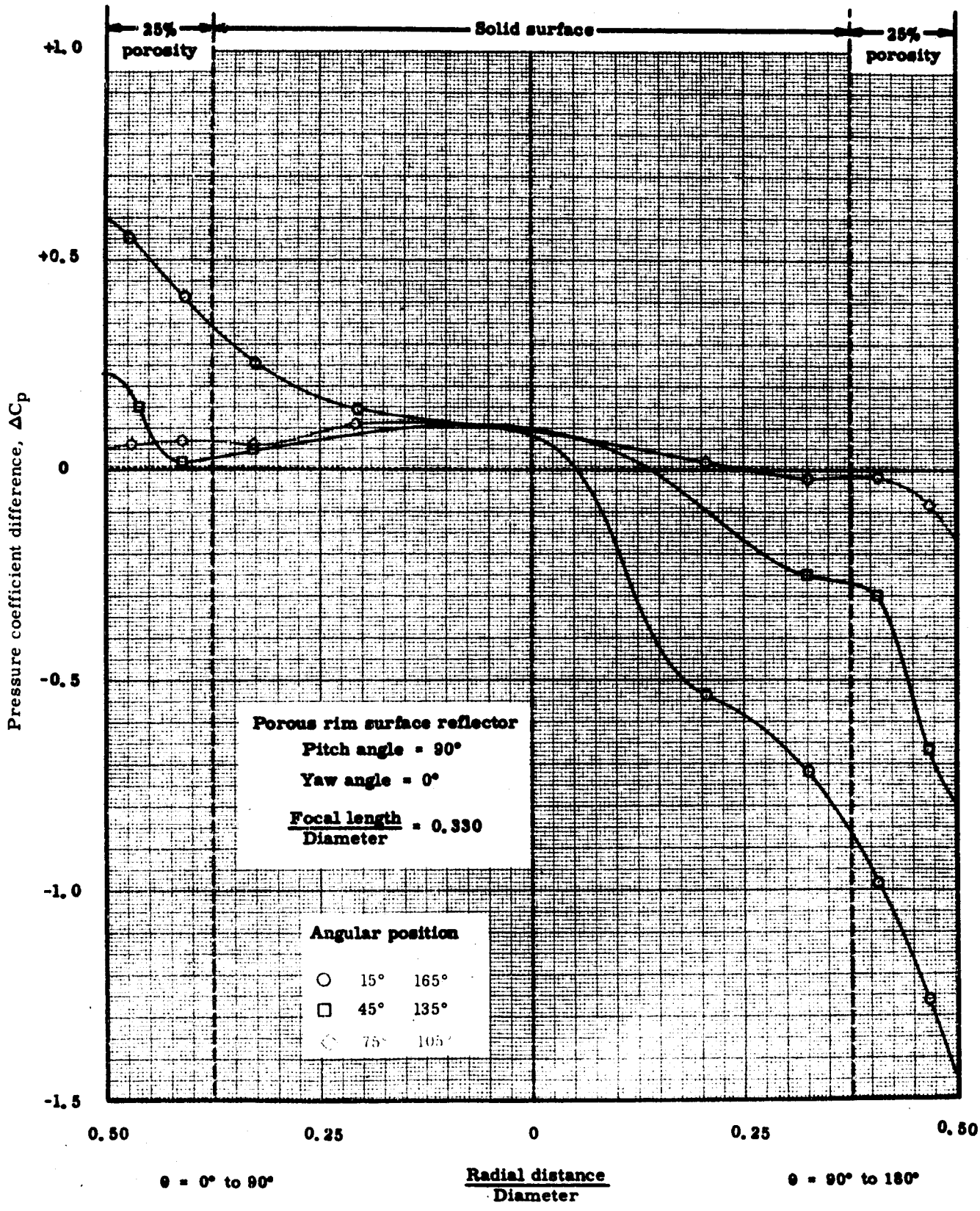

Fig. 12. Pressure Coefficient Difference Across a Thin Paraboloidal Porous Rim Surface, Pitch Angle 90°.

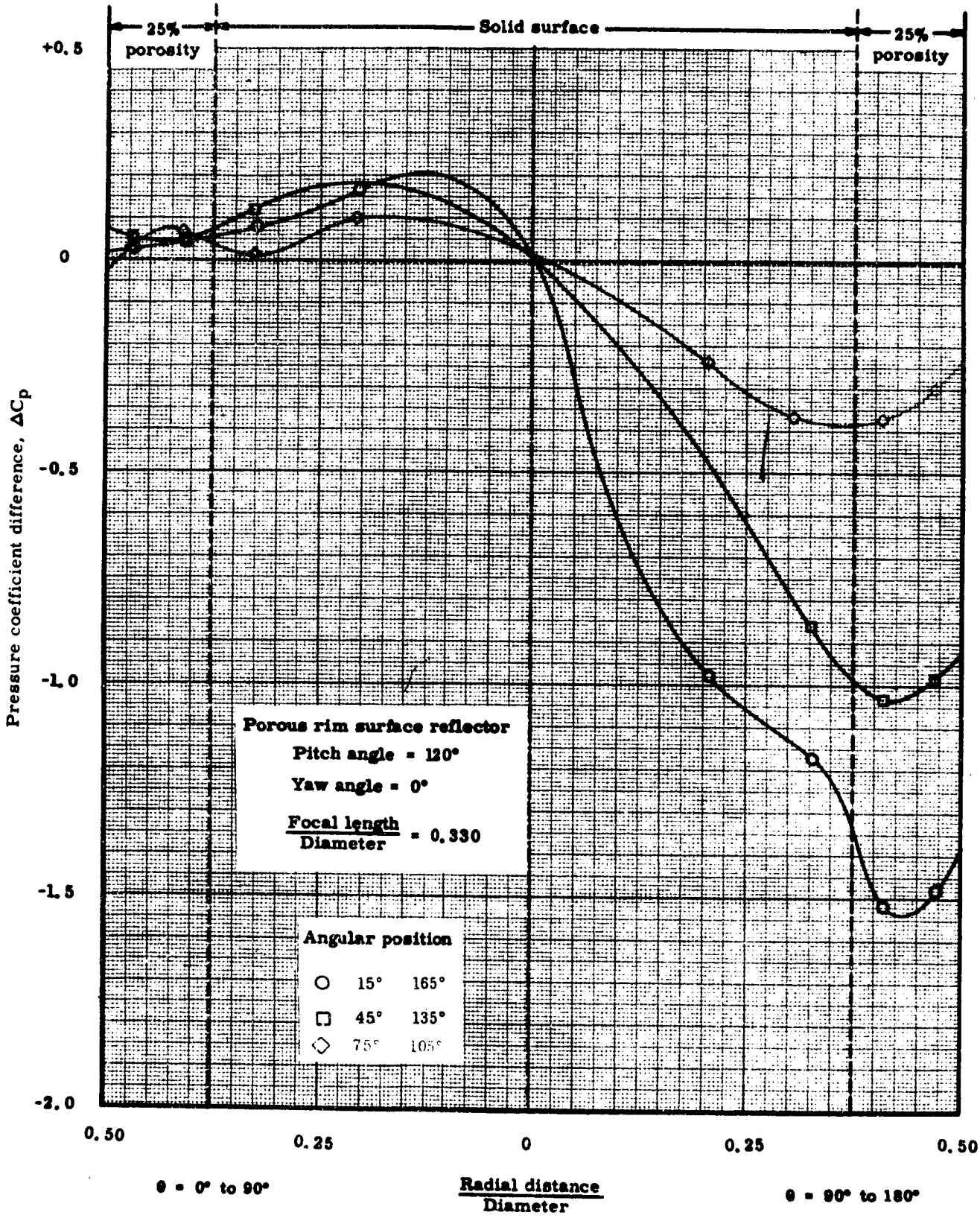

Fig. 13. Pressure Coefficient Difference Across a Thin Paraboloidal Porous Rim Surface, Pitch Angle 120°.

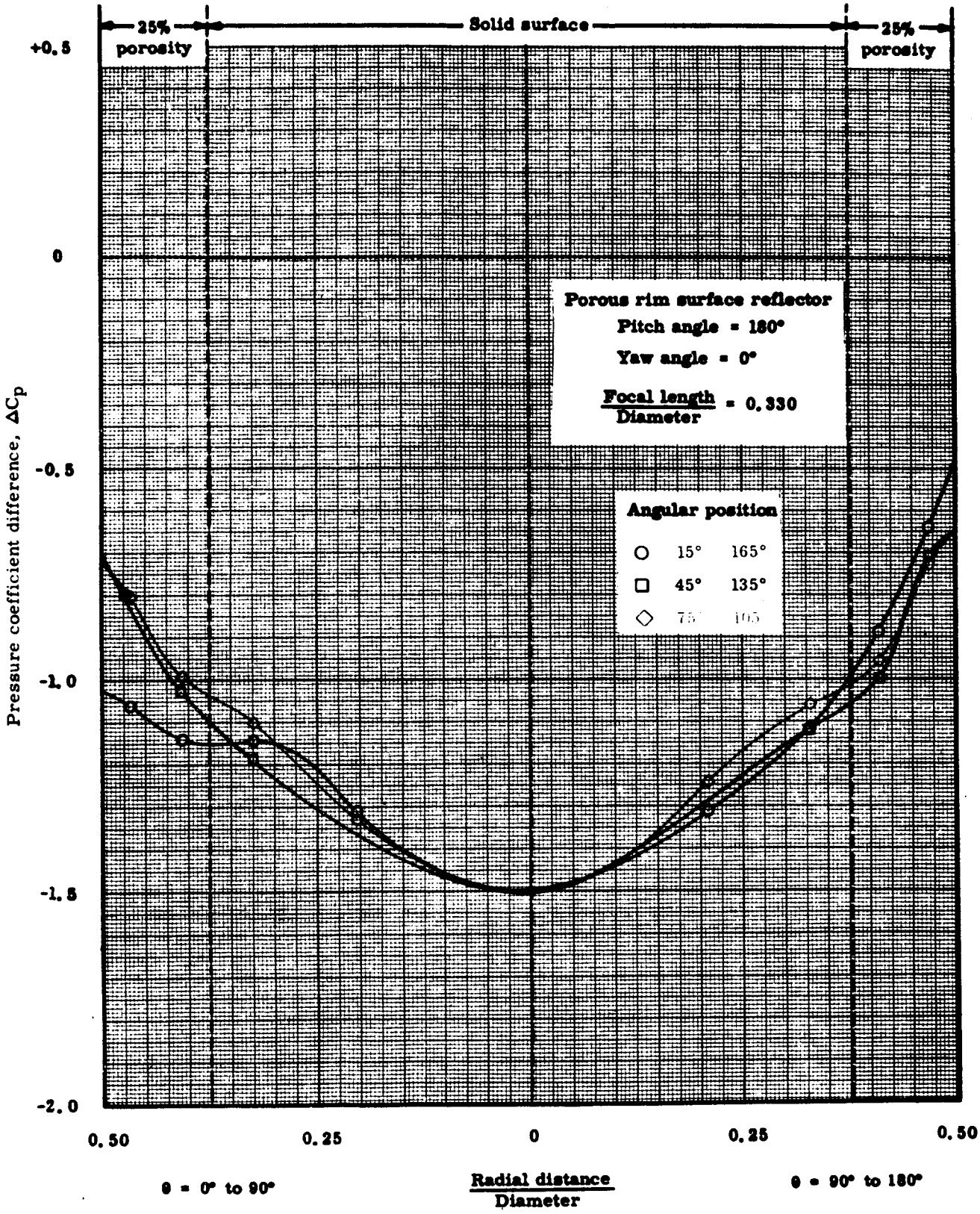

Fig. 14. Pressure Coefficient Difference Across a Thin Paraboloidal Porous Rim Surface, Pitch Angle 180°.

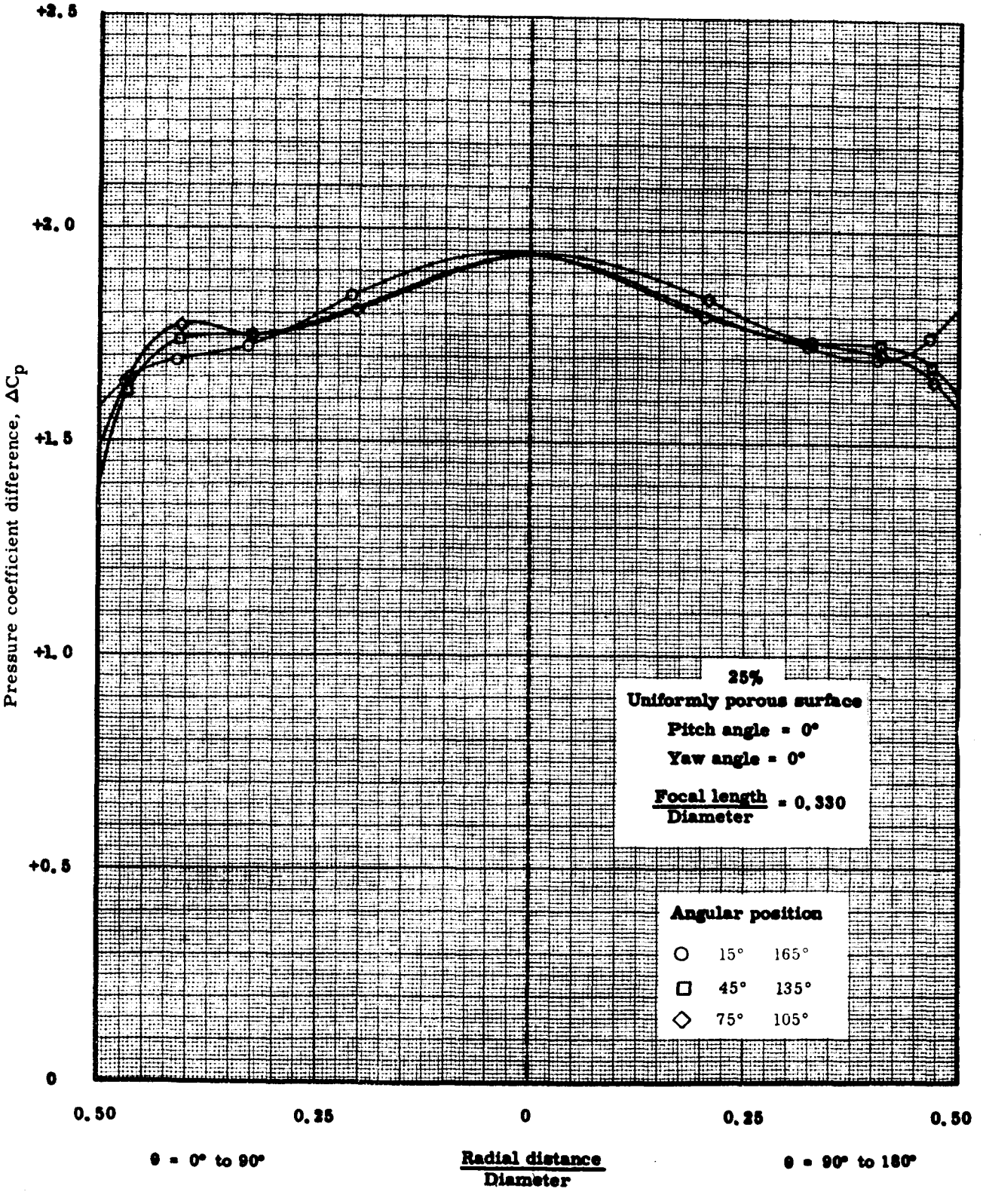

Fig. 15. Pressure Coefficient Difference Across a Thin Paraboloidal Uniformly Porous Surface, Pitch Angle 0°.

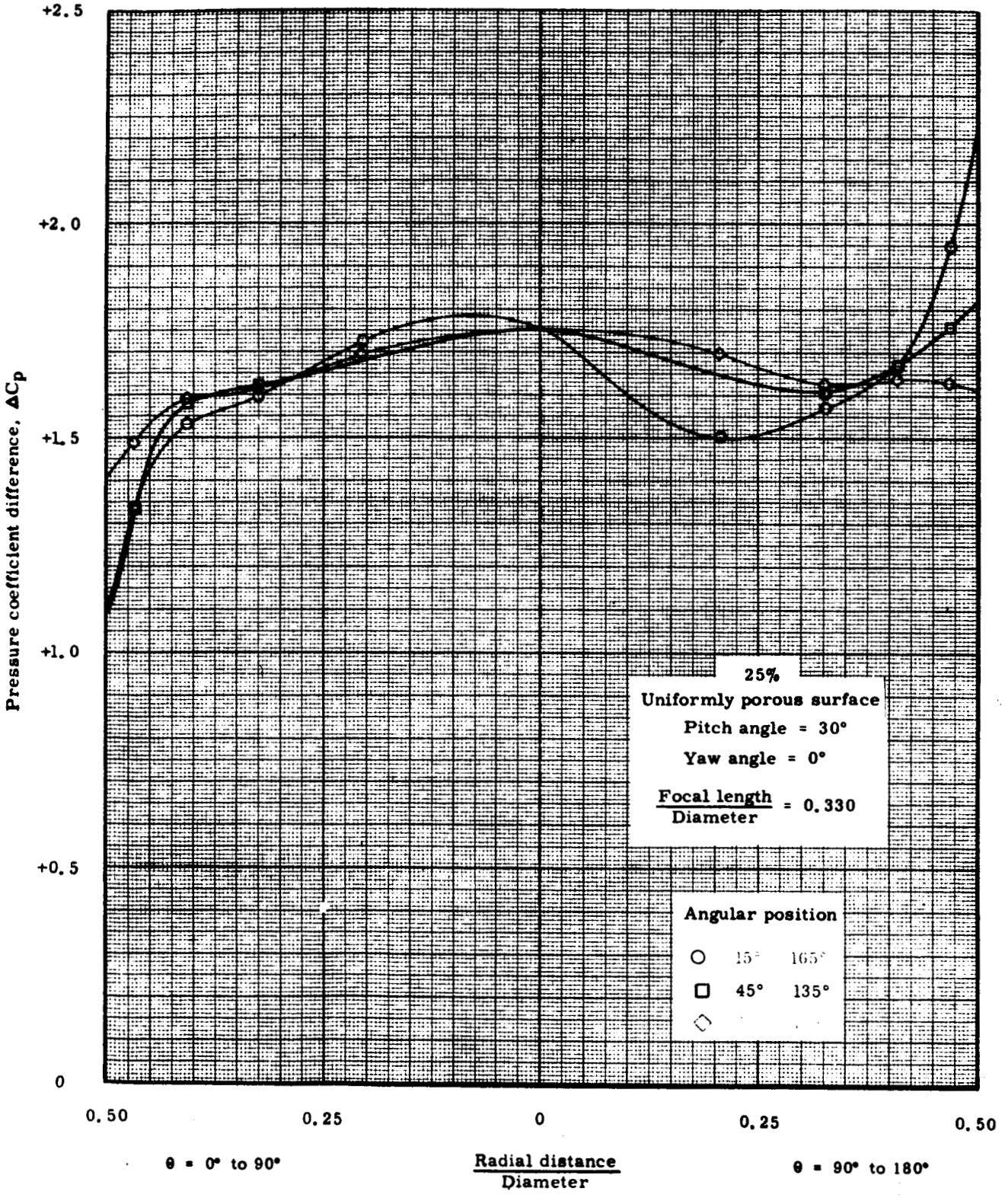

Fig. 16. Pressure Coefficient Difference Across a Thin Paraboloidal Uniformly Porous Surface, Pitch Angle 30°.

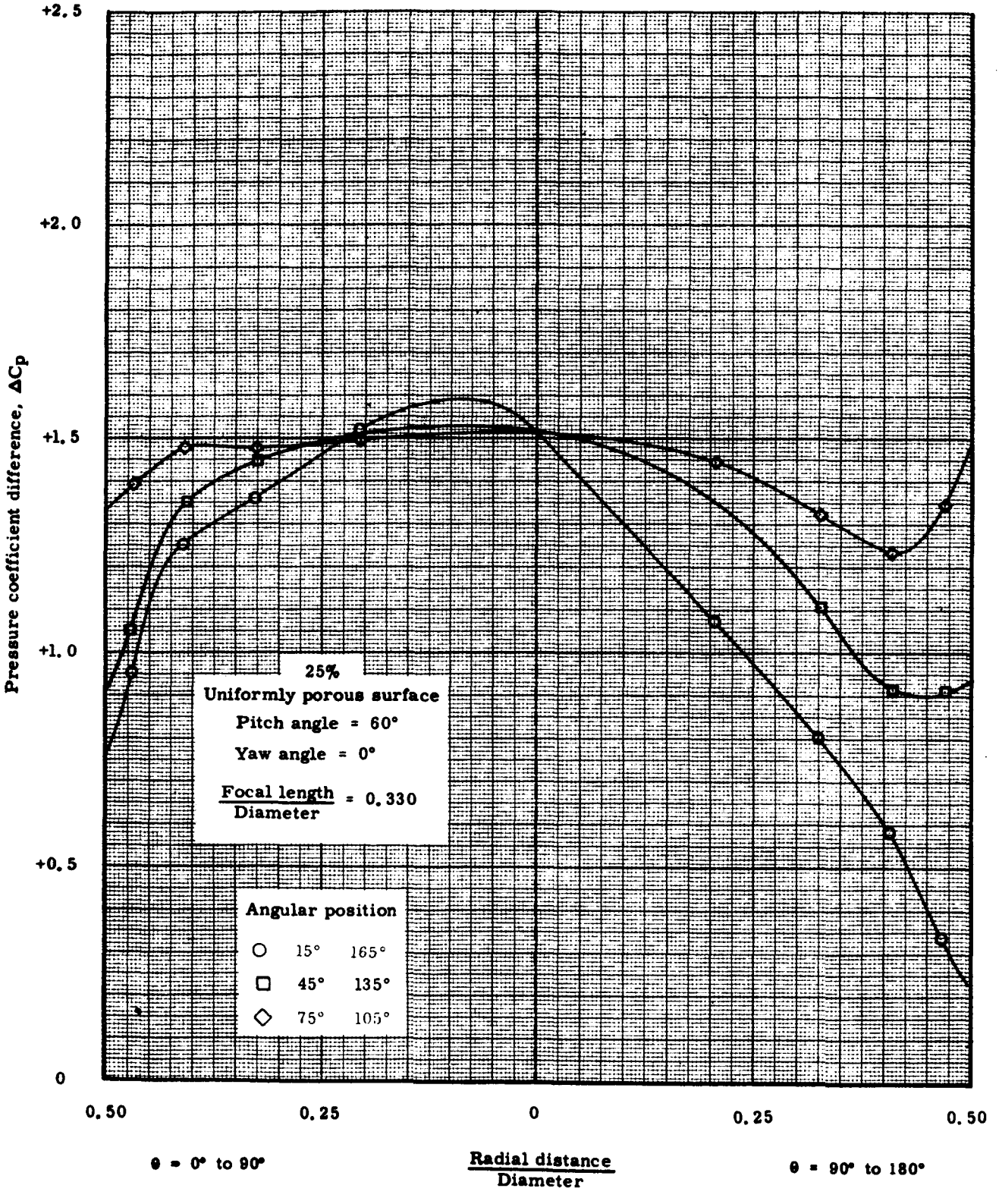

Fig. 17. Pressure Coefficient Difference Across a Thin Paraboloidal Uniformly Porous Surface, Pitch Angle 60°.

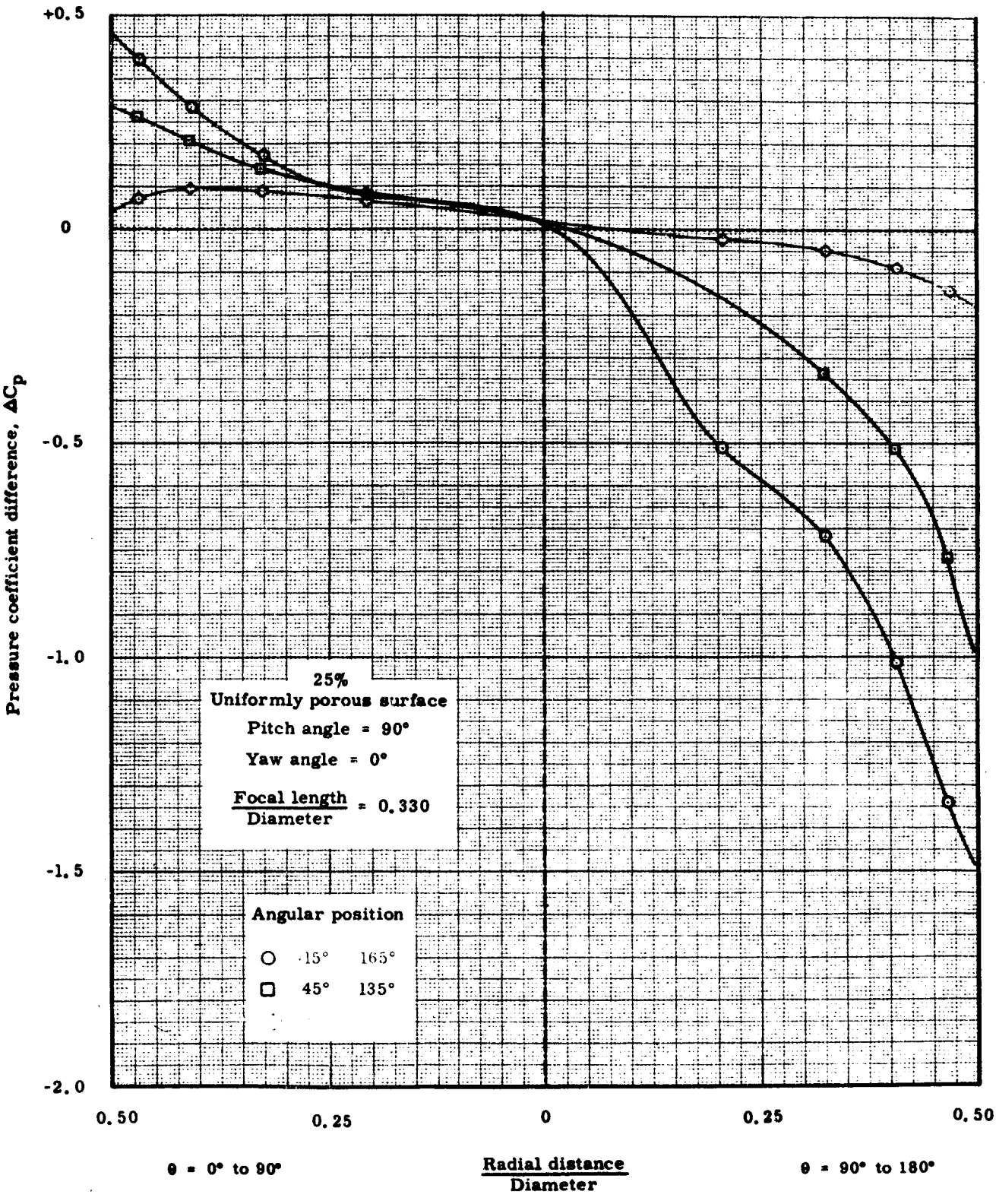

Fig. 18. Pressure Coefficient Difference Across a Thin Paraboloidal Uniformly Porous Surface, Pitch Angle 90°.

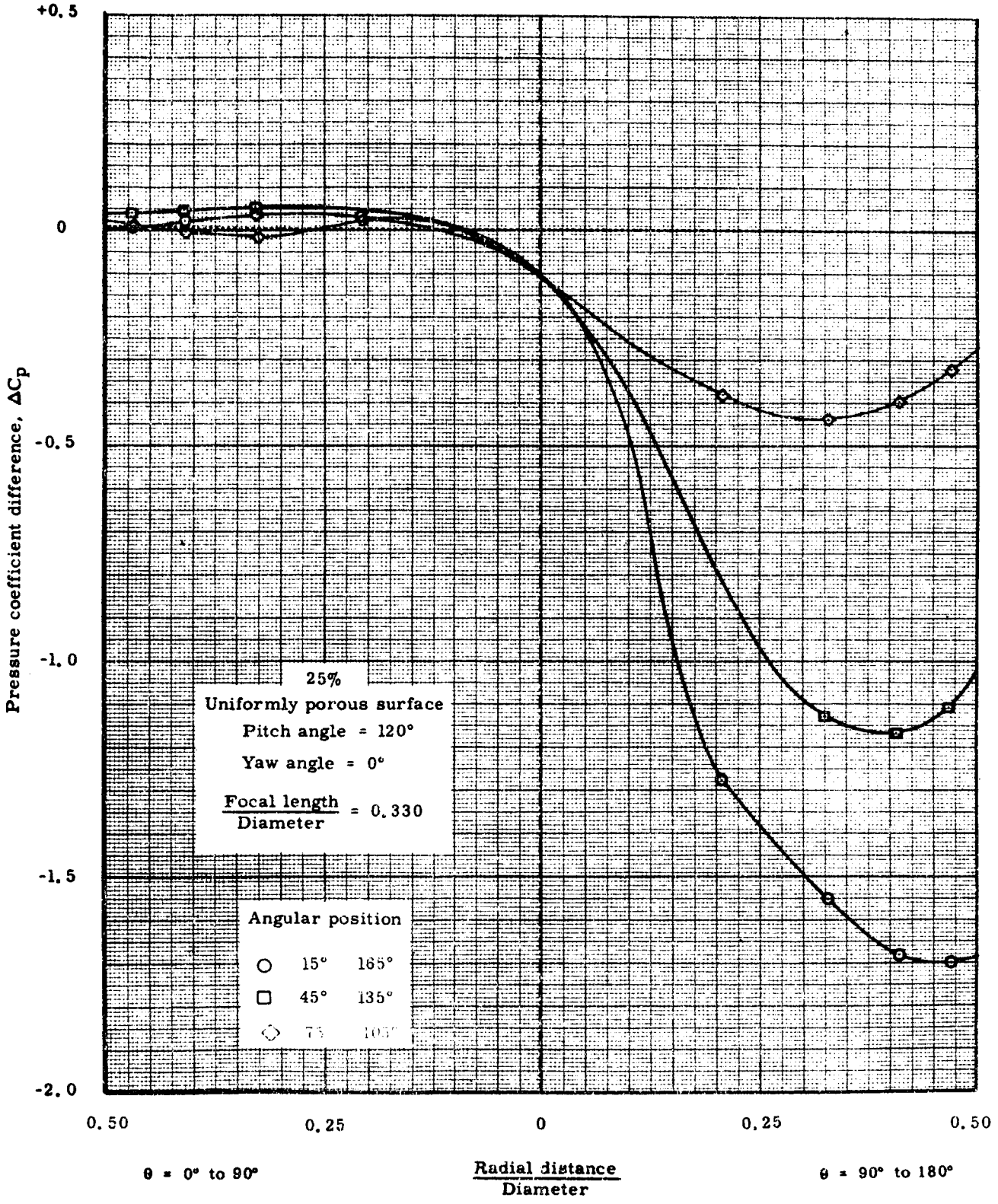

Fig. 19. Pressure Coefficient Difference Across a Thin Paraboloidal Uniformly Porous Surface, Pitch Angle 120°.

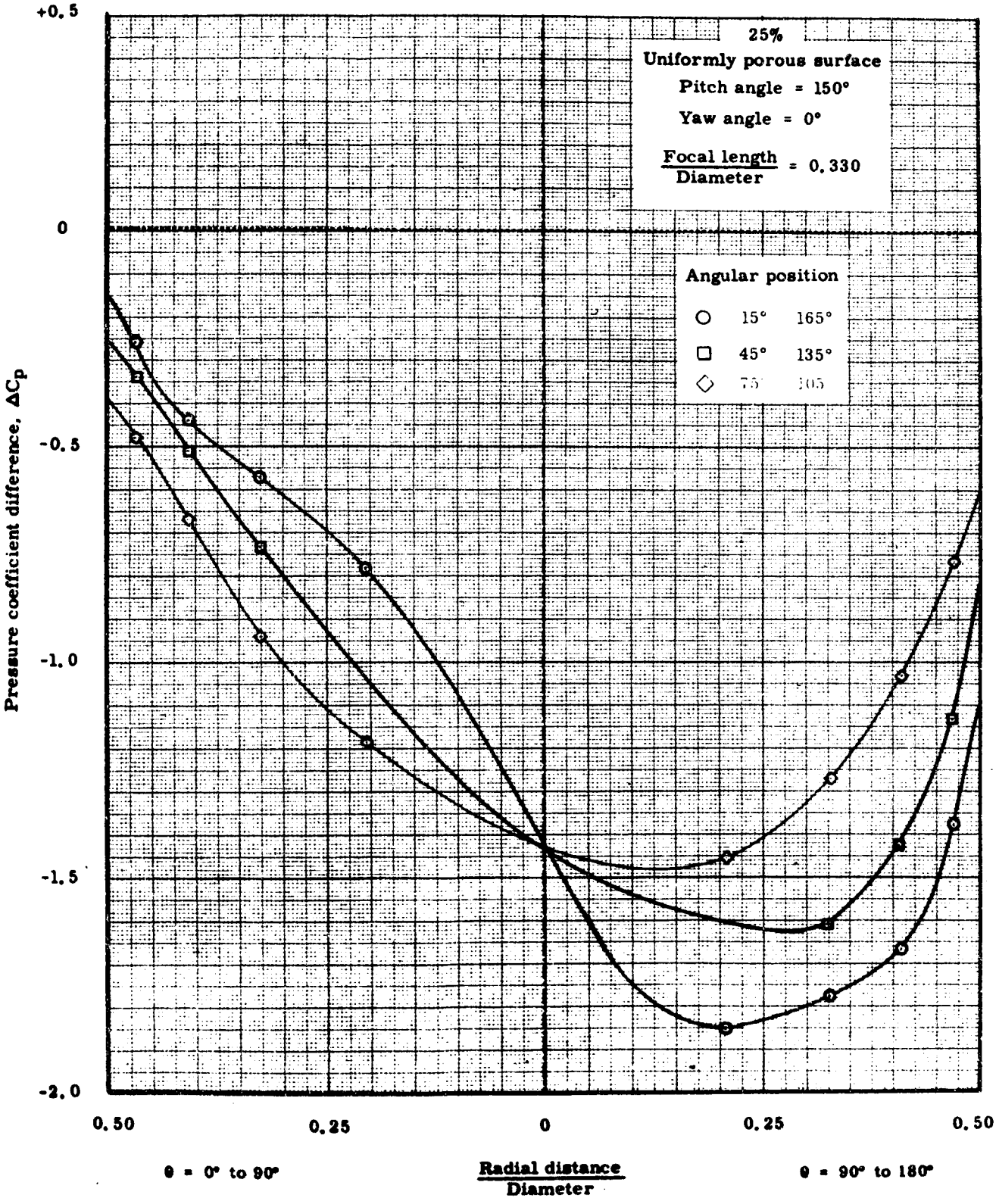

Fig. 20. Pressure Coefficient Difference Across a Thin Paraboloidal Uniformly Porous Surface, Pitch Angle 150°.

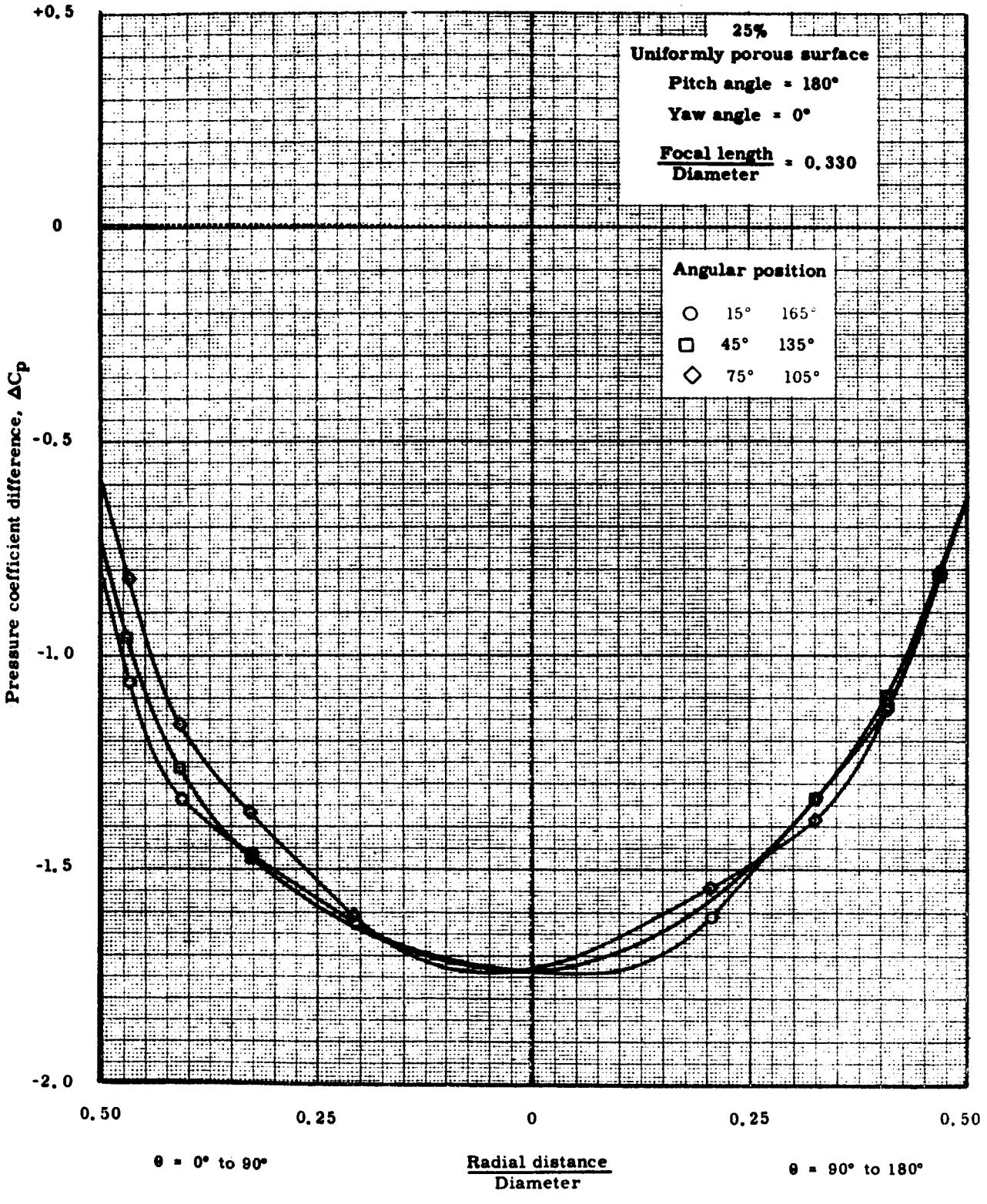

Fig. 21. Pressure Coefficient Difference Across a Thin Paraboloidal Uniformly Porous Surface, Pitch Angle 180°.

Wind direction ⟶

$\frac{\text{Focal length}}{\text{Diameter}} = 0.330$

Edge angle = 53°

Pitch angle = 0°

Yaw angle = 55°

Fig. 22. Antenna Model Being Tested with Yarn Tufts on Convex Surface

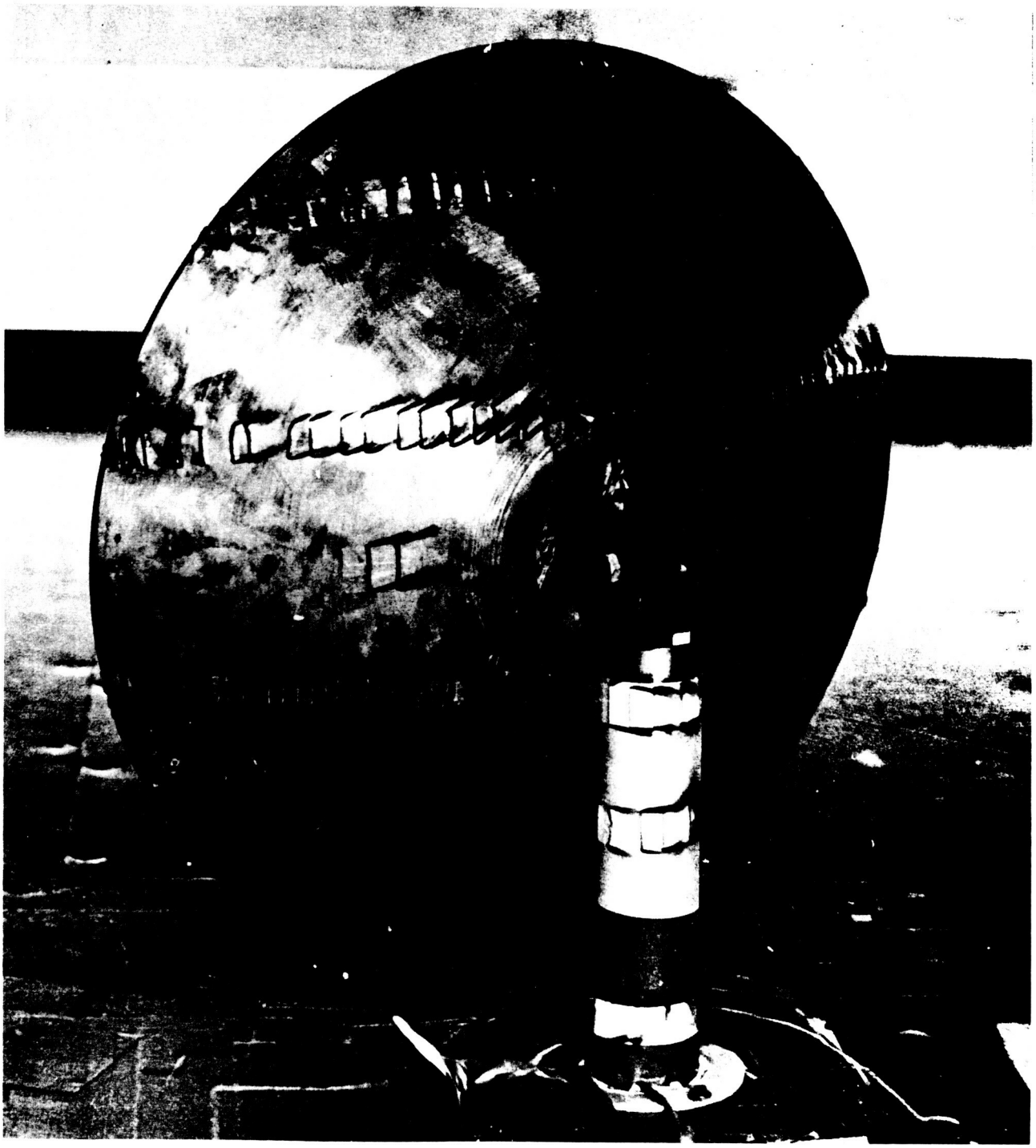

Wind direction →

$\frac{\text{Focal length}}{\text{Diameter}} = 0.330$

Edge angle = 53°

Pitch angle = 0°

Yaw angle = 57.5°

Fig. 23. Antenna Model Being Tested with Yarn Tufts on Convex Surface

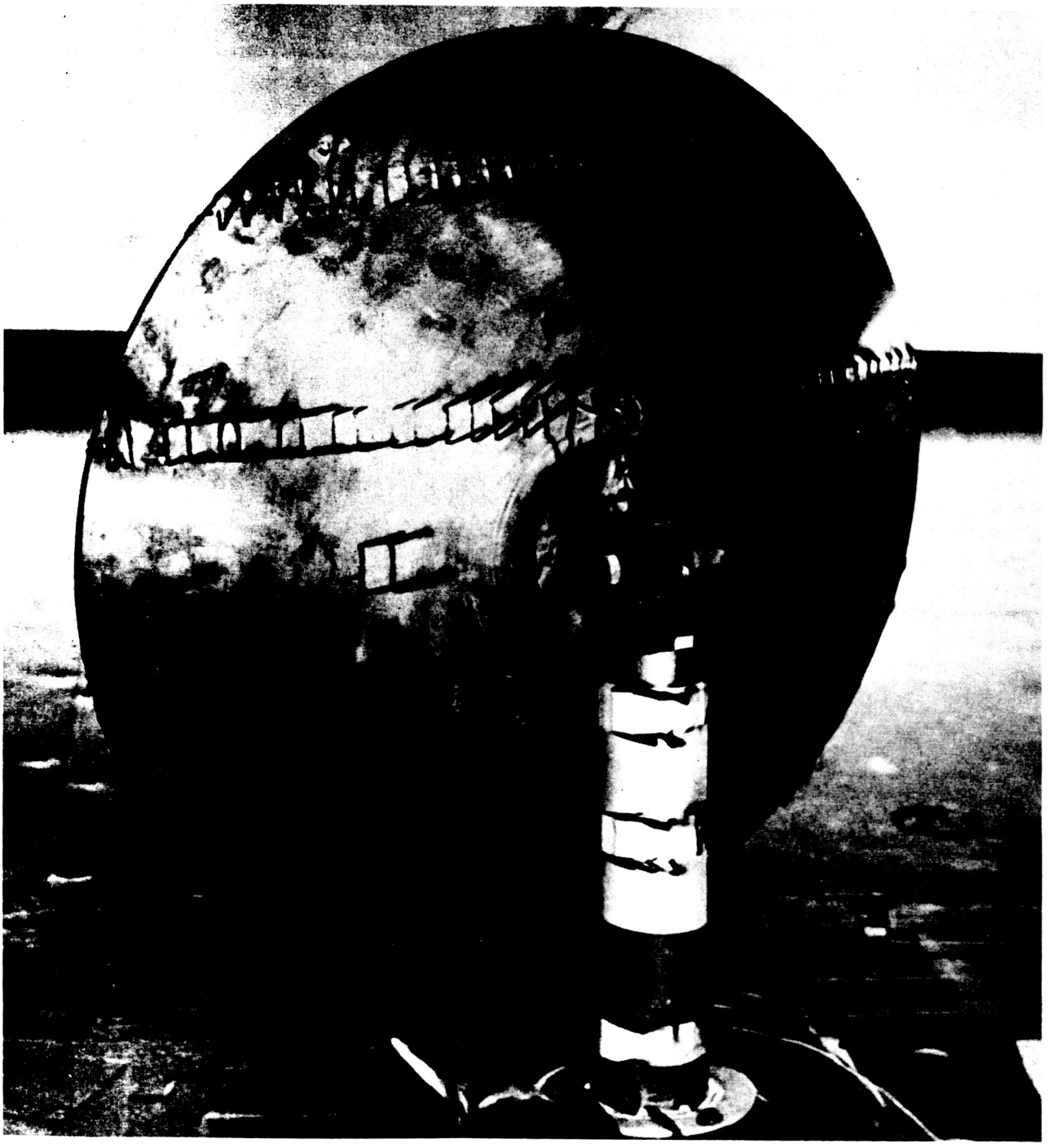

Wind direction ⟶

$\frac{\text{Focal length}}{\text{Diameter}} = 0.330$

Pitch angle = 0°

Edge angle = 53°

Yaw angle = 60°

Fig. 24. Antenna Model Being Tested with Yarn Tufts on Convex Surface

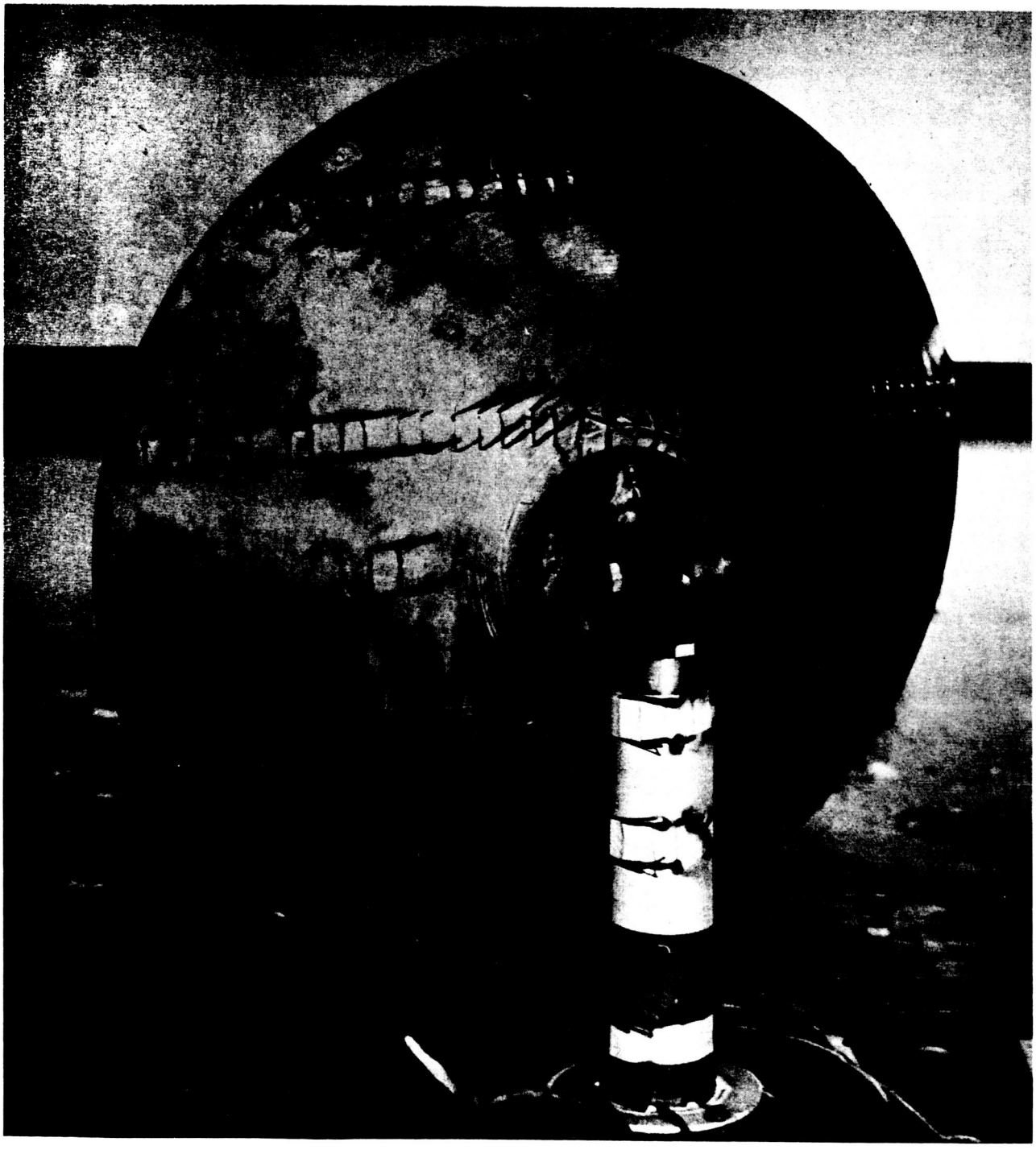

Wind direction →

$\frac{\text{Focal length}}{\text{Diameter}} = 0.330$

Edge angle = 53°

Pitch angle = 0°

Yaw angle = 65°

Fig. 25. Antenna Model Being Tested with Yarn Tufts on Convex Surface

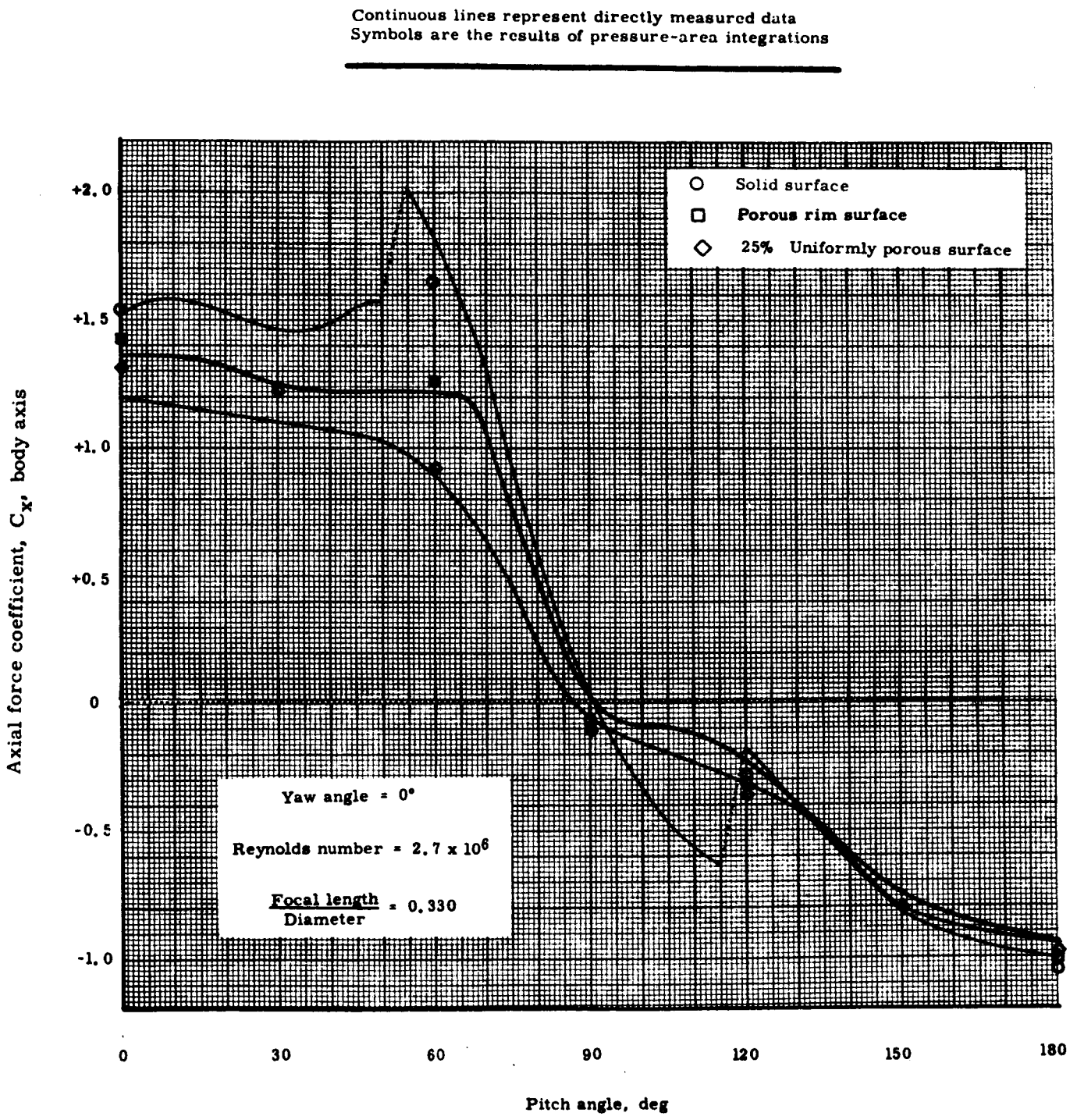

Fig. 26. Comparison of Axial Force Coefficient from Pressure-Area Integrations and Balance Data.

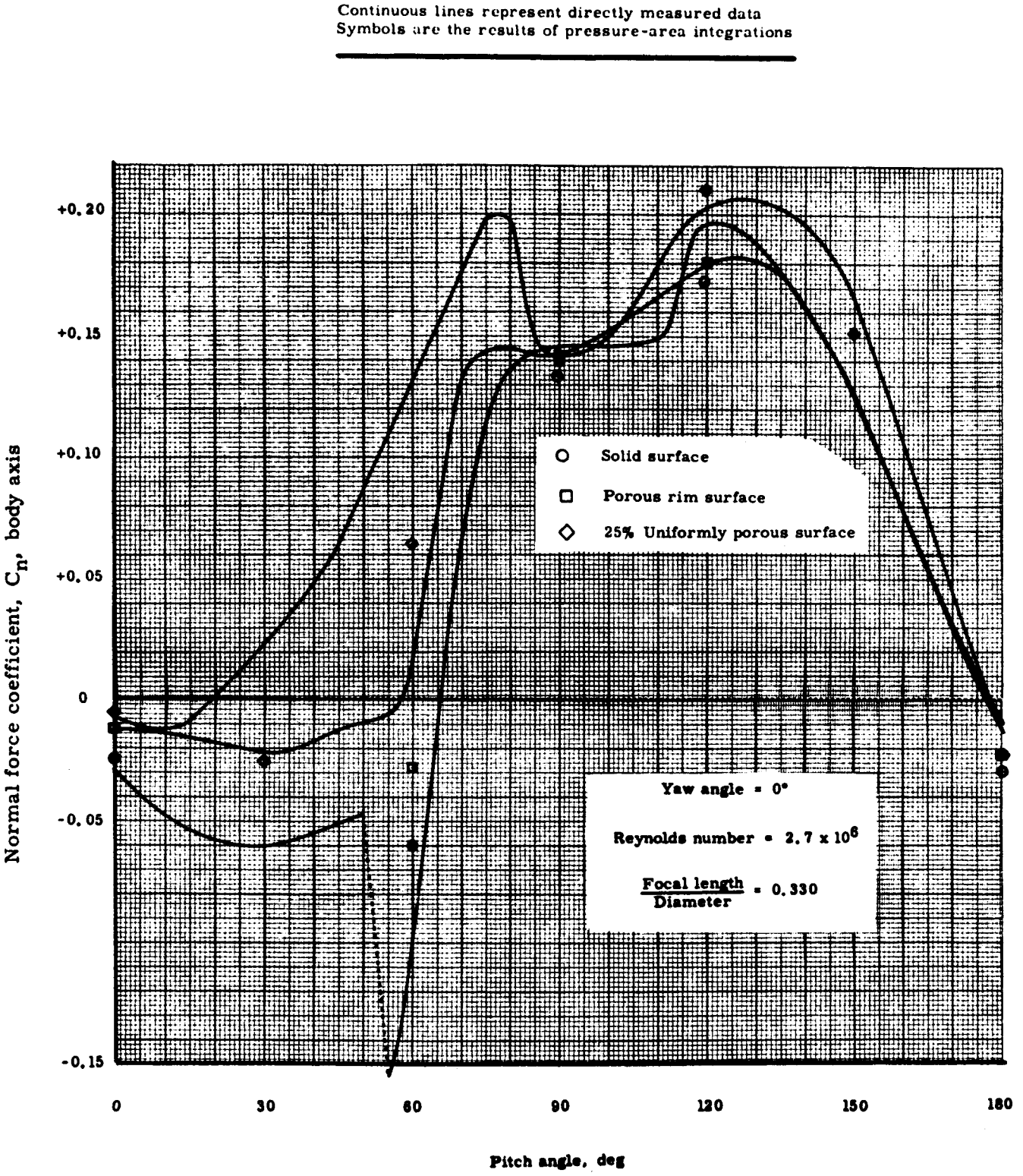

Fig. 27. Comparison of Normal Force Coefficient from Pressure-Area Integrations and Balance Data.

Continuous lines represent directly measured data
Symbols are the results of pressure-area integrations

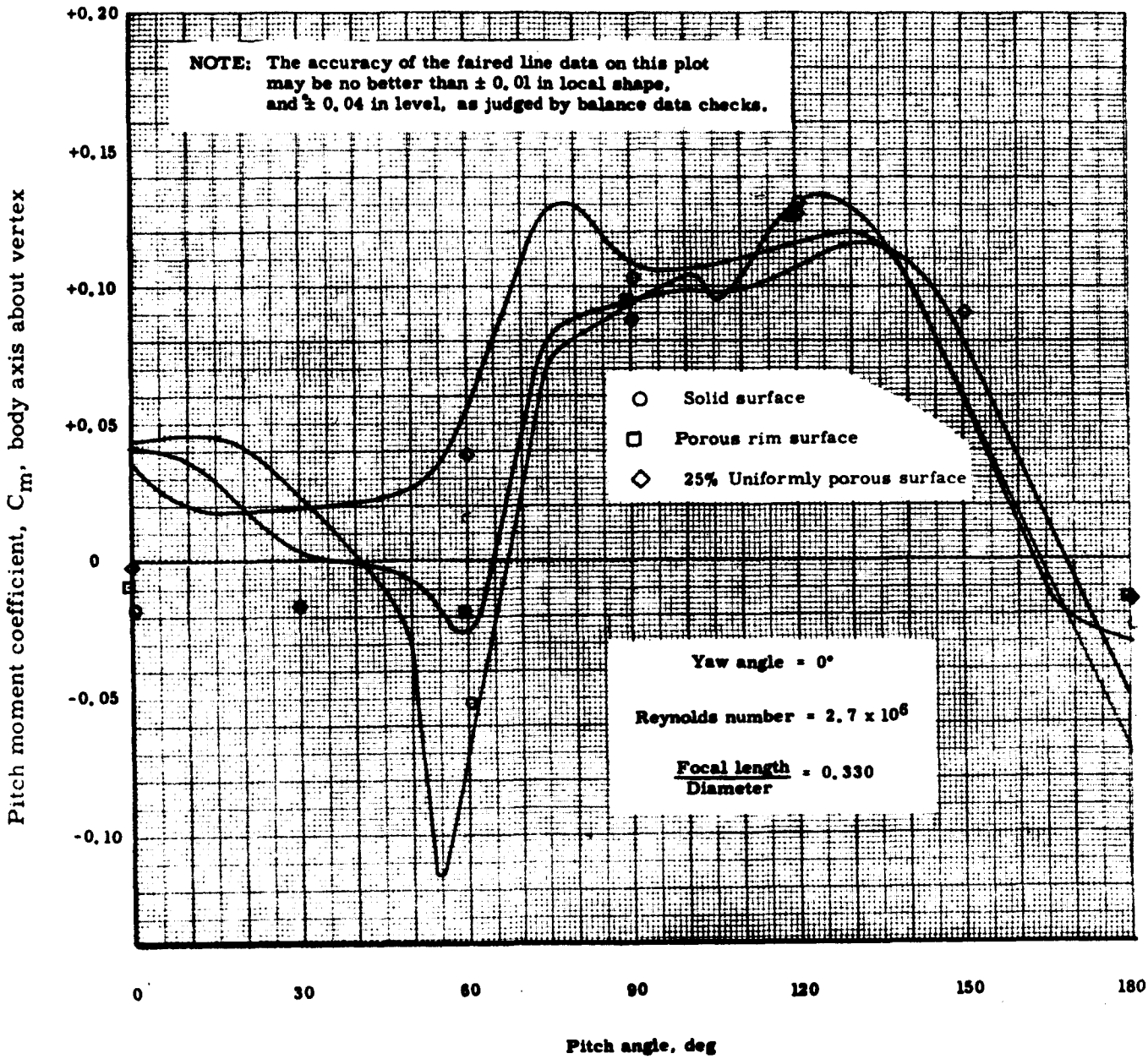

Fig. 28. Comparison of Pitch Moment Coefficient from Pressure-Area Integrations and Balance Data.